

Electrical conductance of single conjugated oligomers

Inauguraldissertation

zur
Erlangung der Würde eines Doktors der Philosophie
vorgelegt der
Philosophisch-Naturwissenschaftlichen Fakultät
der Universität Basel

von

Songmei Wu
aus P.R.China



Genehmigt von der Philosophisch-Naturwissenschaftlichen Fakultät
auf Antrag von
Prof. Dr. C. Schönenberger
Prof. Dr. S. Decurtins
Dr. H. Riel
Dr. M. Calame

Basel, den 5. Jun 2009

Prof. Dr. Hans-Peter Hauri
Dekan

Everyone on earth has a treasure that awaits him.

Paulo Coelho

Chapter 1

Single-molecule electronics: a new view on small molecules

We could all witness the great impact of the development of microelectronics: our electronic devices have been continuously becoming faster, smaller and cheaper. The key driving force is the progressive downscaling of microelectronic building blocks, as predicted by Moore that the number of transistors per chip doubles every two years [1]. This so called “Moore’s Law” successfully remains valid until today. However, the downscaling trend will soon reach its limit due to the principle of current fabrication technology based on lithography. It is already very difficult to make feature sizes below 50 nm. Furthermore, when the feature size reaches a certain scale (\sim tens of nm), quantum phenomena will start to dominate the overall behavior of such structures and new concepts need to be developed to design the devices.

Are there possible alternatives for the development of future electronics? -“There’s Plenty of Room at the Bottom.” In 1959, physicist Richard Feynman presented an inspiring talk in which he proposed making very small circuits out of atoms and small molecules. This is even earlier than the time when the first integrated circuit (IC) was fabricated as a monolithic chip in 1961. A design for a single molecule rectifier based on an electron donor and an acceptor connected by a saturated structure was later suggested theoretically by Aviram and Ratner in 1974 [2].

Although the concept of single-molecule electronics is rather old, it has become only experimentally possible in the last decades thanks to the development of new techniques such as mechanically controllable break junction (MCBJ) [3] and scanning electron microscope (STM) [4], which can form a pair of atomic-sized electrical contacts and a tunable nm-sized gap to wire a single molecule in between. With the variable techniques, single molecules

have recently become the focus of interest.

Individual organic molecules have several advantages as candidates for future nanoelectronics: first of all, they are intrinsically small, typically with length scale of a few nm which is at least an order of magnitude smaller than the features on currently existing microelectronic devices; Secondly, chemists can design molecules with variable functions and produce them in a large amount at low costs by synthetic chemistry. Moreover, the properties of molecules can be tuned and modified by physical or chemical stimuli (for example, electrical potential, light and temperature, etc.). In addition, molecules can self assemble in 2D or 3D supramolecular structures, providing the potential for a bottom-up approach.

As a highly interdisciplinary research field, single-molecule electronics attracts equally the interest of physicists, chemists and material scientists, generating a broad perspective and creative ideas. Due to the small size of single molecules (a few nm), the electron transport through a metal-molecule-metal junction becomes fully quantum and the molecule is discussed in terms of a quantum dot. This opens a new view on simple organic molecules. The effects of molecular inherent characteristics such as backbone structures, contacts, conformations etc. on the electron transport properties are basic issues to understand how such devices could work. It also motivates chemists to build electronic functions such as switching and rectifying in single molecules. Finally, the integration of nm-scale single molecules to outside electrodes remains a demanding task.

Using individual molecules as building blocks for electronic devices opens a worthwhile route for further miniaturization of future electronics. The realization relies on the better understanding and control of charge transport at the level of single molecules.

This thesis

In this thesis we use a mechanically controllable break junction technique to measure the electronic transport properties of single conjugated oligomers. This technique allows precise control of the distance between two atomic-size contacts, matching the size of a molecule. Via a liquid cell we are able to investigate molecules in a controlled liquid environment. Using oligo-phenylene ethynylene (OPE) molecules as our model system, we start with an OPE-dithiol molecule to understand the properties of a metal-molecule-metal junction. To overcome variations in individual conductance traces, we introduce a robust statistical analysis of repeatedly formed molecular junctions. We then move on and study the role of contacts in molecular conductance. Surprisingly, we find out that when one linker group is taken away, clear well-defined molecular signals can still be observed. Finally, we show that conductance of redox molecular junctions can be controlled by an electrochemical gate.

This thesis is structured as follows:

- Chapter 2 introduces theoretical models of the conductance of single molecules.
- Chapter 3 describes the basic principle of mechanically controllable break junctions, the samples and the setup.
- Chapter 4 compares the breaking process in passive pure solvents and to which anchoring molecules are added. On this basis a robust statistical analysis without any data selection will be introduced.
- Chapter 5 discusses the effects of contacts and side groups on molecular conductance.
- Chapter 6 shows a comparison study of an OPE-dithiol and OPE-monothiols.
- In Chapter 7 we demonstrate electrochemical gating at the level of single redox molecules.

Chapter 2

What is the conductance of a single molecule?

The conductance G of a conductor is defined as the ratio between the current passing through it and the applied bias potential ($G \equiv I/V$). The current I increases linearly with applied voltage V and G is constant. This is known as Ohm's law, which is typically valid in macroscopic devices. However, when the size of the conductor decreases, for example, to the extreme of one or several metal atoms, electron transport process changes conceptually. What do we expect and how could we understand the electron transport at such small scale? Furthermore, when a single organic molecule with the size of a few nanometers is sandwiched between electrodes, what is the role of intrinsic properties of molecules and what is the nature of contacts in electron transport through the metal-molecule-metal junction? In this chapter, basic concepts in mesoscopic physics and simple models describing molecular conductance will be introduced.

2.1 A short introduction to organic molecules

Organic molecules are usually composed of carbon atoms in chains, rings, or mixture of both, to which other element atoms such as hydrogen, oxygen, sulfur and nitrogen are attached. They have infinite possible structures in synthetic chemistry, and different structures give various properties and functions to the molecular building blocks.

Shown in Fig. 2.1 are some examples of small molecules which have typical length of 1 nm. An alkane molecule (Fig. 2.1a) has a simple structure containing only carbon and hydrogen atoms. Due to the rotation of the carbon-carbon sigma bond, an alkane molecule can have trans- and gauche-

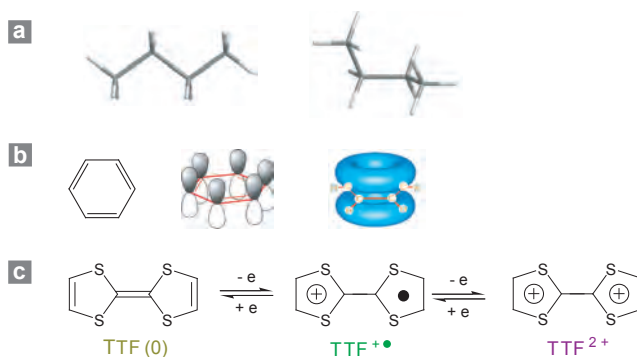


Figure 2.1: Examples of small molecules (a) an octane molecule with trans-(left) and gauche-(right) conformations; (b) a conjugated benzene molecule; (c) a tetrathiafulvalene (TTF) molecule with redox property.

conformations. In a benzene ring (Fig. 2.1b), there are three extra alternate π -bonds formed between carbon atoms. As a result, the 6 π -electrons are fully delocalized in the molecular backbone. Such a structure is called conjugation, and it can also be formed in a chain shape such as polyacetylene. The molecule in Fig. 2.1c contains sulfur atoms in the ring structure. This tetrathiafulvalene (TTF) molecule possesses well known redox properties. By chemical or electrochemical oxidation, it can lose one electron to turn into radical cation state and lose two to become a dication [5]. These processes are fully reversible. It is not only the small size of the molecules but also their intrinsic characters that make them interesting candidates for electron transport studies.

In molecular physics, molecules are described by molecular orbitals, which are wave functions as mathematical solutions to the Schrödinger equation. Molecular orbitals specify the spatial distribution and energy of up to two electrons within it.

Let us take a simple hydrogen molecule as an example. The wavefunction which describes the two electrons for a pair of hydrogen atoms H_a and H_b can be symmetric or antisymmetric. As shown in Fig. 2.2, when the two hydrogen atoms are brought close together the symmetric spatial wavefunction Ψ_s leads to an overlap configuration of electrons and the antisymmetric one Ψ_a forms a destructive configuration. The actual electron charge density is given by the square of the magnitude of the wavefunction. The symmetric wavefunction gives a high electron density between the nuclei, leading to a

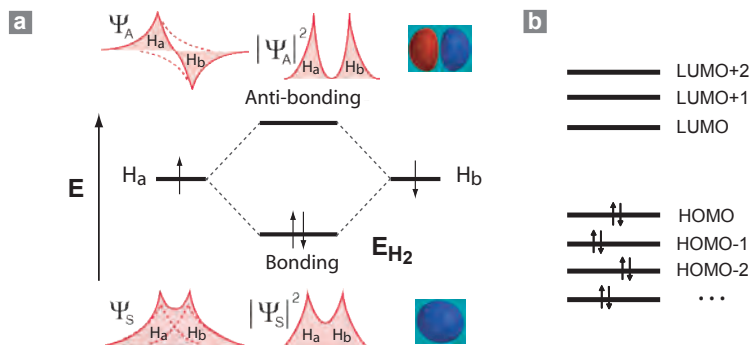


Figure 2.2: Schematic illustration of molecular orbitals: (a) an example of bonding and antibonding orbitals of a hydrogen molecule (wavefunction picture is adapted from HyperPhysics); (b) HOMO and LUMO orbitals of a generic organic molecule.

net attractive force between the atoms, forming a lower energy orbital for hydrogen molecule which is called bonding orbital. In contrast, the asymmetric wavefunction leads to a higher energy orbital which is called anti-bonding orbital.

For a generic organic molecule, interactions between different atomic orbitals give rise to many discrete molecular orbitals. Electrons occupy the orbitals according to the Pauli principle up to a certain energy level which is called the highest occupied molecular orbital (HOMO), whereas the lowest empty level is called the lowest unoccupied molecular orbital (LUMO). The energy gap in between is called HOMO-LUMO gap, similarly to the band gap of a semiconductor.

The value of the HOMO-LUMO gap depends mainly on the structure of the molecule. Saturated molecules such as alkanes are composed of sigma bonds, where electrons tend to localize on carbon atoms, leading to large HOMO-LUMO gap (~ 7 eV). For conjugated molecules, due to the delocalization of π -electrons, the HOMO-LUMO gap is rather small (~ 3 eV). HOMO-LUMO gap of a conjugated molecule can be measured by UV-vis absorption spectroscopy. The absorption peaks for the smallest bonding π to anti-bonding π^* transitions are in an experimentally convenient region of the spectrum (200 – 700 nm).

2.2 Conductance quantization of an atomic-sized junction

In a macroscopic conductor, electrons travel in a diffusive way. This means that electrons get frequently scattered by collisions with obstacles such as impurities and grain boundaries (Fig. 2.3a). The average distance which an electron travels between two scattering events is known as the elastic mean free path ℓ . The conductance is characterized by the classical Ohm's law. The conductance G is directly proportional to the transverse area A and inversely proportional to the sample length L . G is given by:

$$G = \frac{\sigma A}{L}, \quad (2.1)$$

where the conductivity σ is a scale independent material property.

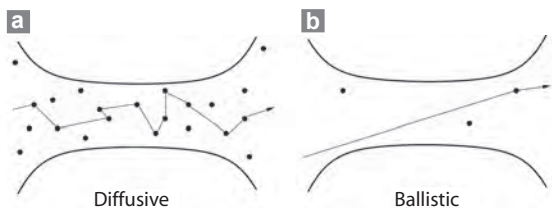


Figure 2.3: Schematic illustration of (a) a diffusive and (b) a ballistic conductor.

However, when the length scale of the conductor becomes smaller than the elastic mean free path ($L < \ell$), electron transport process changes from diffusive to ballistic in which the electron momentum can be assumed to be constant and only limited by scattering with the boundaries of the sample (Fig. 2.3b). Therefore the classical Ohm's law is no longer valid.

For an atomic-sized contact of a metal, the contact width W is of the order of a few nanometers or even less and thus W is comparable with de Broglie wavelength λ_F . We therefore enter into the full quantum limit [6]. In this regime, Landauer viewed current flow as a transmission process, or a consequence of the injection of carriers at the contacts and probability of the carriers to reach the other end [7; 8]. This approach has proven to be extremely useful for transport properties of nanostructured materials and devices, including molecular systems.

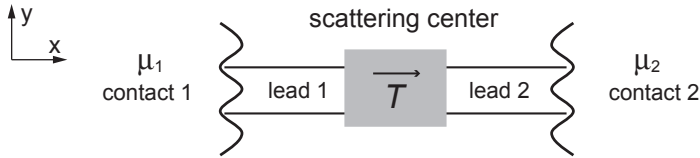


Figure 2.4: A 1D conductor having a transmission probability T is connected to two large contacts through two leads.

Landauer formula: conductance from transmission

Let us consider a metallic, one dimensional conductor, in contact with two electron reservoirs through two leads (Fig. 2.4). The contacts have different chemical potentials μ_1 and μ_2 by applying a small voltage difference V , i.e., $\mu_1 - \mu_2 = eV$. If we assume $\mu_1 > \mu_2$, electrons are flowing from the first reservoir to the second. At $T = 0$ K, the resulting current is given by:

$$I = e \int_0^\infty v(k) n(k) f_1(1 - f_2) dk - e \int_0^\infty v(k) n(k) f_2(1 - f_1) dk, \quad (2.2)$$

with m the electron mass, \hbar the reduced Plank constant, $f(k)$ the Fermi function, the electron group velocity $v(k) = \hbar k / m$, and the density of state between k and $k + dk$, including electron spin, $n(k)dk = 2 \cdot \frac{1}{L} \cdot \frac{L}{2\pi} dk$, we then get:

$$I = \frac{2e}{h} (\mu_1 - \mu_2) = \frac{2e^2}{h} V. \quad (2.3)$$

By definition of the conductance ($G \equiv I/V$) we obtain the quantum conductance unit $G_0 = 2e^2/h = 77.5 \mu\text{S}$. This result holds for one dimensional systems in which only one conduction channel (or mode) exists in the direction normal to the propagation. In general, in addition to many channels, scattering can take place and the conductance of the conductor has to be characterized by a transmission function T where several conduction channels can contribute to. The expression of conductance becomes [7; 8]:

$$G = \frac{2e^2}{h} \sum_{ij} T_{ij}. \quad (2.4)$$

This is called Landauer formula, where T_{ij} is the probability that a carrier

(e.g. electron) transmits from the i_{th} mode at the left of the conductor to the j_{th} mode at the right of the conductor. The actual number of modes is determined by the valence orbital structure of the atoms, which is between 1 and 3 for most metals. Known as an s -metal, gold has only a single valence orbital [6]. Therefore the conductance of a single Au atom contact is G_0 . The Landauer formula tells us that if we could deform a ballistic conductor to vary the number of channels, we should see steps in the conductance. This is called conductance quantization [9; 10].

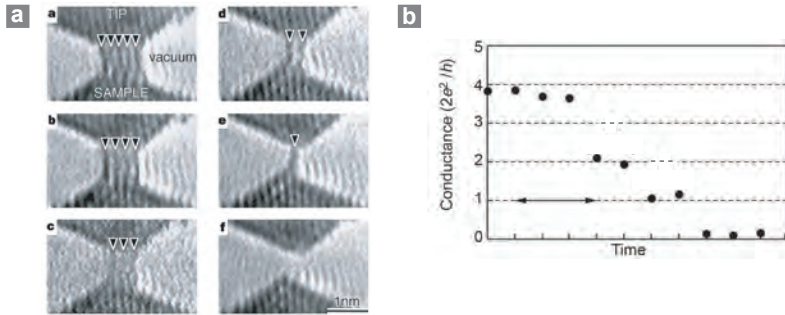


Figure 2.5: (a) Electron microscope images of a contact while withdrawing the tip. A gold bridge formed between the gold tip (top) and gold substrate (bottom), thinned from *a* to *e* and ruptured at *f*. Dark lines indicated by arrowheads are rows of gold atoms. (b) Conductance quantization of a contact while withdrawing the tip. [11]

Such conductance quantization has been observed by various experiments. For example, Ohnishi *et al.* use a miniaturized scanning tunneling microscope in ultrahigh-vacuum and the Au tip could be simultaneously imaged by high-resolution transmission electron microscope (TEM), which allows direct observation of the relation between electron transport and structure of the Au bridge [11]. During the stretching of the Au tip, the constriction becomes thinner and thinner. They could observe strands of gold atoms that are about one nanometer long and sequentially break one strand after another till the bridge is completely open (Fig. 2.5a). Correspondingly the conductance shows quantized plateaus and the last plateau has the value of G_0 (Fig. 2.5b).

An explanation of the overall resistance

Related to the value of G_0 , there is still a remaining question. Since electrons transport ballistically in a single atom conductor, the resistance should be nearly zero in this range. How do we then understand the large overall resistance ($R_0 = 1/G_0 = 12.9 \text{ k}\Omega$) of an atomic contact? The proper interpretation of this result was first pointed out by Imry [12], who associated the finite resistance with the resistance arising at the interfaces between the leads and the contacts.

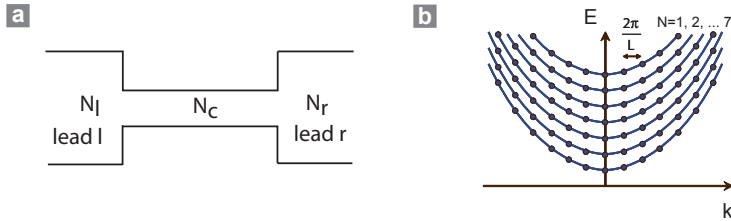


Figure 2.6: (a) Schematic illustration of a one dimensional conductor connected to two large contacts through two wide cylindrical leads. N_c is the number of propagating modes at the Fermi energy in the constriction, N_l and N_r are the modes on the left and right leads. (b) Dispersion relations for electrons with N the number of propagating modes ($= 7$ in this case).

Take the example of a conductor with a narrow constriction connected to two large contacts through two wide cylindrical leads as shown in Fig. 2.6a. On these leads, the electrons propagate as plane waves along the longitudinal direction, while its transverse momentum is quantized due to the lateral confinement, leading to several subbands. The energy dispersion relation $E_i(k_i)$ in the i -th subband (Fig. 2.6b) is:

$$E_i(k_i) = E_i^0 + \frac{\hbar^2 k_i^2}{2m^*}, \quad (2.5)$$

with m^* the effective mass of electrons.

This quantization defines a set of incoming and outgoing modes on each contact. If N_c is the number of propagating modes at the Fermi energy in the constriction, N_l and N_r are the modes on the left and right leads. In such a geometry, contact leads contain large number of modes but only a few can get through the constricted section, which results in a large contact resistance [6].

The contact resistance can be probed by a four-terminal resistance mea-

surement. Picciotto *et al.* have reported that ballistic 1D wires of 2D electron gas indeed show a vanishing resistance [13]. This demonstrates experimentally that the high resistance values observed in two-probe measurements on such systems originate from the contacts alone, and that the intrinsic resistance is negligible.

2.3 Modeling the conductance of a molecular junction

If a metallic point contact breaks and separates to form a pair of atomically sharp tips, these tips can be used as electrical contacts to small molecules. Practically molecules are usually designed to have terminal linker groups which allow to bind chemically to electrodes to form metal-molecule-metal junctions. It is then possible to measure their transport properties. We will introduce several models here to describe the conductance of a molecular junction.

2.3.1 Single molecules as electron tunneling barrier

In this model a single molecule is sandwiched between two metal contacts. The role of the molecule is considered as tunneling barrier for electron transport. It is also called superexchange model [14; 15].

First let us view the situation in which electrons tunnel between two conductors through vacuum (Fig. 6.3a). When electrons are incident upon a vacuum barrier with potential energy larger than their kinetic energy, incoming electrons are mostly reflected but there is still a non-zero probability that they may traverse the forbidden region and reappear on the other side of the barrier. If the two conductors are close enough, with a small bias voltage, a resulting current, I , will flow across the vacuum gap.

The tunneling effect originates from the wavelike properties of electrons. A quantum mechanic treatment predicts an exponential decaying solution for the electron wave function in the barrier. The transmission probability under low bias potential (up to several hundred mV) is given by:

$$T = e^{-\beta d}, \quad (2.6)$$

with d the barrier width and β the tunneling decay parameter in unit of $(\text{length})^{-1}$.

Using the Landauer Formula (eq. 2.4) one can estimate the conductance through a tunnel junction as:

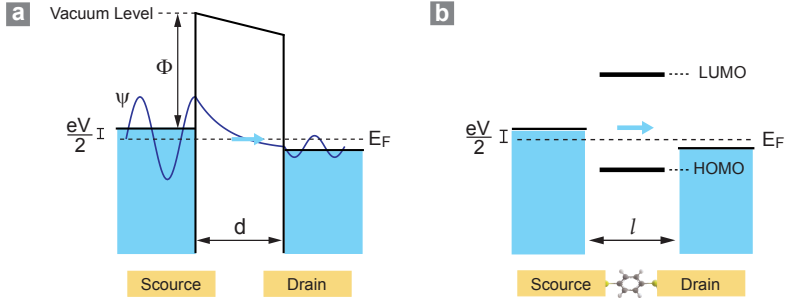


Figure 2.7: Schematic of electron tunneling through: (a) vacuum; and (b) a 1,4-benzene dithiol molecule.

$$G = G_0 \cdot e^{-\beta d}; \text{ with } \beta = \frac{2\sqrt{2m(\Phi - \frac{eV}{2})}}{\hbar}, \quad (2.7)$$

where m is the electron mass, Φ is the local tunneling barrier height in vacuum (= work function for metals), V is the applied bias voltage between the two contacts. If the applied voltage is much smaller than the work function ($eV \ll \Phi$), the tunneling decay parameter can be simplified to $\beta = \frac{2\sqrt{2m}\Phi}{\hbar}$.

Taking a work function value for gold 5.0 eV, the decay factor for electrons tunneling in vacuum is $\beta_{vacuum} = 1.025\sqrt{\Phi} [\text{eV}^{-0.5} \text{\AA}^{-1}] = 2.3 \text{\AA}^{-1}$.

As an example, a 1,4-benzene dithiol molecule can be sandwiched between source and drain electrodes as shown in Fig. 6.3b. The molecule has defined discrete energy levels (the most important levels for transport are HOMO and LUMO orbitals). The conductance G_{mol} can in analogy be written as [16]:

$$G_{mol} = A \cdot e^{-\beta l}; \text{ with } \beta = \frac{2\sqrt{2m^*\Phi^*}}{\hbar}, \quad (2.8)$$

where l is the length of molecule, m^* is the effective electron mass and Φ^* is the effective tunneling barrier height. The prefactor A depends on the electron density-of-states at the point where the molecule contacts the gold electrode. Instead of the work function in vacuum, the tunneling barrier amounts to the closest molecular level related to E_F of the metal [17; 18],

i.e. $\Phi^* = (E_F - E_{LUMO})$ or $\Phi^* = (E_{HUMO} - E_F)$. For a simple estimation that E_F locates in the middle of HOMO-LUMO gap and there is no broadening and charging effects, the tunneling barrier Φ^* can be written as $\Phi^* \simeq (E_{HOMO} - E_{LUMO})/2$.

As mentioned before, conjugated molecules (Fig. 2.1b) have smaller HOMO-LUMO gap than saturated molecules (Fig. 2.1a), therefore lower tunneling decay factor ($\sim 0.3 \text{ \AA}^{-1}$) compared with saturated alkanes ($\sim 1 \text{ \AA}^{-1}$).

2.3.2 Electron hopping through a single molecule

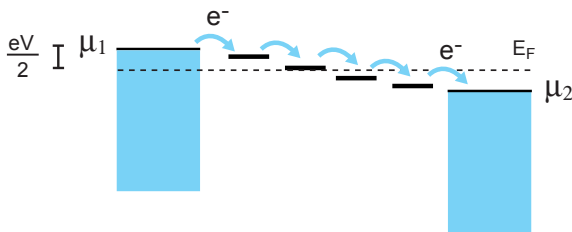


Figure 2.8: The model of electron hopping through the states of a long molecular wire.

When the length of molecular bridges increases, the charge transport mechanism changes then from direct tunneling to hopping. For a long molecular “wire”, electrons dwell on several molecular orbital states and the transport is therefore incoherent. This is evidenced by a change in the length dependence of the electron transfer rate [19]. Specifically, for short bridges, the length dependence is exponential according to tunneling as discussed in Section 2.3.1. For long bridges with hopping mechanism, the scaling is linear. Furthermore, the two mechanisms show different behaviors on temperature dependence: The tunneling process is temperature independent, while hopping is strongly thermally activated.

Experimentally, the transition between the two mechanisms can be observed by measuring the conductance change of molecular junctions with different molecular length built by the same repetition unit and at different temperatures. A metal-coated atomic force microscope (AFM) technique was used to measure the resistance and current-voltage characteristics of conjugated molecular wires ranging in length from 1 to 7 nm. The tunneling to hopping transition was observed at the length of ~ 4 nm. [20]

2.3.3 Resonant double barrier tunneling model

In this model a single molecule sandwiched between two metal electrodes is represented by one energy level. The electron transport can be calculated by using simple kinetic equations. However when a molecule binds chemically to electrodes through terminal linker groups, the molecule can not be treated as an isolated system as in vacuum anymore. The coupling of the molecule to electrodes leads not only to the broadening but also to a shift of the molecular energy levels. These aspects will be discussed in the following sections.

Single level model

A simple resonant tunneling model [21] can be introduced by considering only one discrete molecular energy level ε being close to the Fermi energy E_F (Fig. 2.9).

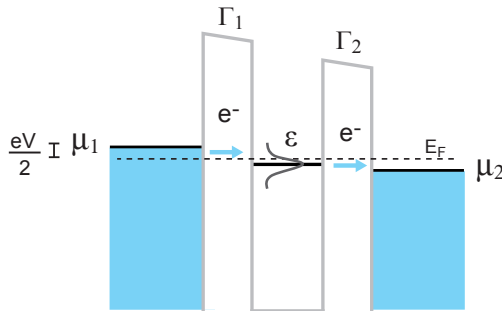


Figure 2.9: The model of electron tunneling through a double barrier Γ_1 and Γ_2 . The molecule is represented by one discrete molecular energy level ε being close to the Fermi energy E_F and it is broadened by coupling to electrodes.

Unlike the superexchange model as described in Section 2.3.1, here electrons at this resonant energy level ε can cross the double barrier without being reflected. The current through the level can then be derived sequentially. The numbers of electrons occupying the level would be given by $N_1 = 2f(\varepsilon, \mu_1)$ if the level is in equilibrium with the left contact and by $N_2 = 2f(\varepsilon, \mu_2)$ in equilibrium with the right one. The factor 2 comes from the spin degeneracy, and $f(\varepsilon, \mu_i)$ is the Fermi-Dirac function. In non-equilibrium, the number N of electrons in the level will be somewhere in between N_1 and N_2 . We can write the resulting current from the left con-

tact to the molecule:

$$I_1 = \frac{e\Gamma_1}{\hbar}(N_1 - N), \quad (2.9)$$

and from the molecule to the right contact as:

$$I_2 = \frac{e\Gamma_2}{\hbar}(N - N_2). \quad (2.10)$$

Γ_1 and Γ_2 have the dimension of energy, denoting the coupling between the contacts and the level. Γ_1/\hbar and Γ_2/\hbar have the dimension of s^{-1} . They are the rates at which an electron will escape initially from the source contact to the level ε and from the level to drain contacts respectively. In equilibrium, I_1 must be equal to I_2 so that

$$N = \frac{N_1\Gamma_1 + N_2\Gamma_2}{\Gamma_1 + \Gamma_2}, \quad (2.11)$$

and finally we get the net current:

$$I = I_1 = I_2 = \frac{2e}{\hbar} \frac{\Gamma_1\Gamma_2}{\Gamma_1 + \Gamma_2} [f(\varepsilon, \mu_1) - f(\varepsilon, \mu_2)]. \quad (2.12)$$

Knowing the energy level ε , the coupling factors Γ_1, Γ_2 and the electrochemical potentials μ_1, μ_2 of the two contacts, we can calculate the current I from eq. 2.12.

This simple result serves to illustrate certain basic facts about the process of current flow. Firstly, no current will flow if $f(\varepsilon, \mu_1) = f(\varepsilon, \mu_2)$. A level ε that is way below both electrochemical potentials μ_1 and μ_2 will have $f(\varepsilon, \mu_1) = f(\varepsilon, \mu_2) = 1$, and way above both potentials, $f(\varepsilon, \mu_1) = f(\varepsilon, \mu_2) = 0$. In both cases, the level ε will not contribute to the current. It is only when the level lies within a few $k_B T$ of the potentials μ_1 and μ_2 that we have $f(\varepsilon, \mu_1) \neq f(\varepsilon, \mu_2)$. Contact 1 keeps pumping in electrons and contact 2 keeps pulling them out, resulting a continuous transfer of electrons from contact 1 to 2 corresponding to a current I in the external circuit.

Broadening of molecular levels

For a metal-molecule-metal junction, if the molecule is strongly coupled to the metallic contacts, the molecular orbitals and the electronic states of the leads can overlap. This leads to a hybridization of the electronic states, and therefore a common delocalized electronic wave function extending over the whole junction. In consequence the density of states $D(E)$ (the probability of having an electron state with energy E) can not be described anymore by a Dirac delta function at energy ε . The total broadening of the single

energy level is $\Gamma = \Gamma_1 + \Gamma_2$ and is better represented by a Lorentzian density of states [21] as shown in Fig. 2.9:

$$D(E) = \frac{1}{2\pi} \frac{\Gamma}{(E - \varepsilon)^2 + (\Gamma/2)^2}. \quad (2.13)$$

Including this in eq. 2.12 and integrating over the energy we finally obtain the current:

$$I = \frac{2e}{\hbar} \int_{-\infty}^{\infty} dE T(E) [f(\varepsilon, \mu_1) - f(\varepsilon, \mu_2)], \quad (2.14)$$

where the transmission function T is defined as:

$$T(E) = 2\pi D(E) \frac{\Gamma_1 \Gamma_2}{\Gamma_1 + \Gamma_2} = \frac{\Gamma_1 \Gamma_2}{(E - \varepsilon)^2 + (\Gamma_1 + \Gamma_2)^2/4}. \quad (2.15)$$

At low temperatures, we can rewrite eq. 2.14 as:

$$I = \frac{2e}{\hbar} \int_{-\mu}^{\mu} dE T(E), \quad (2.16)$$

with $\mu = +eV/2$ and $-\mu = -eV/2$. In the linear regime ($eV \rightarrow 0$), the expression for the conductance is then

$$G = \frac{2e^2}{\hbar} \frac{\Gamma_1 \Gamma_2}{(E - \varepsilon)^2 + (\Gamma_1 + \Gamma_2)^2/4}. \quad (2.17)$$

Charging effects

When a molecule is chemically bonded to metal electrodes, a partial charge-transfer takes place even without having an applied bias voltage. Therefore, the charge on the molecule differs from that of an isolated molecule in vacuum. The additional charging energy, U_c describes how the molecular levels are shifted in energy by a contact potential due to electrons lost or gained by the molecule upon coupling to the leads. The molecular level is therefore shifted to ε' :

$$\varepsilon' = \varepsilon + U_c, \quad (2.18)$$

with ε being the energy level of the isolated molecule. This modified energy can be inserted into eq. 2.13 to express the density of states including charging effects:

$$D(E) = \frac{1}{2\pi} \frac{\Gamma}{(E - \varepsilon - U_c)^2 + (\Gamma/2)^2}. \quad (2.19)$$

Depending on the coupling term Γ , $D(E)$ can deviate significantly from the ideal shape of Lorentzian distribution. If the molecule is weakly coupled to the metallic contacts ($\Gamma \ll U_c$), the junction behaves as a capacitor. After one electron tunnels onto the molecule, the capacitor is charged with charging energy $E_C = e^2/2C$. If the capacitance is very small, the energy buildup can be large enough to prevent another electron from tunneling in. The electrical current is then suppressed at low bias voltages and charge transport occurs in integer values of the charge quantum e . It is called Coulomb blockade. This phenomenon can be observed at temperatures where the characteristic charging energy is larger than the thermal energy of the charge carriers ($E_C > k_B T$).

Chapter 3

MCBJ: Making electrical contacts to single molecules

To determine the electronic properties of molecular junctions, molecules need to be wired between a source and a drain electrode. It is a real experimental challenge to form stable and reproducible contacts with defined spacing on the 1 nm scale without damaging or altering the molecules.

There have been development of new techniques in the last decade which allow to gently form metallic contacts to molecules. Some examples are shown in Fig. 3.1. (a) Transfer printing is used to make top electrodes to self assembled monolayers (SAM) [22]; (b) Nanoparticals are taken to bridge the gap which is larger than the length of molecules [23]; and (c) Au colloids can form 2D arrays of molecular networks [24]. In these approaches, the molecular junctions usually encompass few hundreds to several thousands of molecules, therefore the single molecule information is largely averaged. To quantify the properties of a particular molecular junction, the number of molecules in the junctions has to be estimated.

In comparison, a scanning tunneling microscope (STM) break junctions [25] has advantages for studying the charge transport at the level of single molecules. As schematically shown in (d), a tunable sub-nm sized gap is formed when the tip electrode first touches the substrate surface and is then moved up. During the stretching process, a single or a few molecules with terminal anchor groups can bridge the gap to form a molecular junction. This technique also provides reproducible breaking and reformation of molecular junctions which makes statistical analysis possible.

We use mechanical controllable break junction (MCBJ) in our single-molecule measurements (Fig. 3.2). It forms a pair of atomically sharp contacts and a sub-nm gap similarly as in STM break junctions. An important

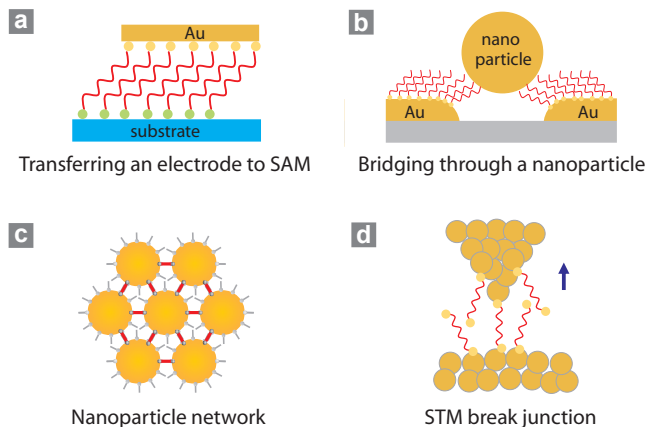


Figure 3.1: Examples of techniques which allow to connect molecules to macroscopic electrodes: (a) Contacting molecular SAM by a transferred electrode: the molecules can have different chemical linker groups to the top electrode and the substrate material. It is possible to first assemble molecules on the substrate and then “print” the top electrode by a metal-coated stamp; (b) Bridging molecules between the nanogap through a nanoparticle; (c) A two dimensional Au colloids network is firstly stabilized by saturated alkane monothiols (gray rods) and the target conjugated molecules (red rods) are then inserted and interlinked inbetween by molecular exchange; (d) STM break junction with a tunable gap size to access the electron transport properties of single molecules.

feature of this technique is that it can provide precise control of the gap size at the picometre scale with high mechanical stability. These advantages led to a wide use of the MCBJ in molecular electronics. Experiments in liquid [3; 26; 27; 28; 29; 30], vacuum [31; 32], argon atmosphere [33], at low temperature [34; 35; 36; 37; 38; 39; 40], or in combination with a UV light source [41] or a Raman spectrometer [42] have been reported.

The principle, sample fabrication and setup used in our mechanical break junction experiments will be described in detail in this chapter. Furthermore, in order to access properties of redox molecules, the adaption of the setup and the sample fabrication to electrochemical-break junctions will also be introduced.

3.1 The principle: Forming atomic contacts by breaking a metal wire

Atomic-size contacts can be obtained by a simple experimental technique called mechanically controllable break junction (MCBJ): A conventional break junction sample is made manually by soldering a thin Au wire with diameter of several hundred micrometers on a flexible substrate. The center of the wire is notched under a microscope by a scalpel, making a freestanding constriction at the center. Then the sample is mounted in a bending apparatus and held by two counter supports. While pressing the substrate from below, the constriction gets continuously stretched and eventually breaks, resulting in two atomically sharp-tip electrodes as schematically shown in Fig. 3.2.

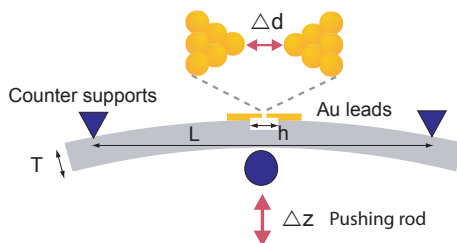


Figure 3.2: Principle of a mechanically controllable break junction. While bending the substrate the metallic constriction breaks, forming a pair of atomic sized contacts. After breaking of the Au wire the horizontal separation distance Δd between the two electrodes can be further adjusted by vertical movement of the push-rod Δz .

After breaking of the Au wire the horizontal separation distance Δd between the two electrodes can be further adjusted by vertical movement of the push-rod Δz . These two tips can also be fused again by relaxing the bending of the substrate. For the ideal case of an elastically homogeneous bending beam with supported ends, the model of mechanical “3-point bending mechanism” tells us that the gap size Δd is proportional to the push-rod movement Δz . The relation of the two axial movements is given by an attenuation factor a :

$$a = \frac{\Delta d}{\Delta z} = \frac{6Th}{L^2}, \quad (3.1)$$

with T the thickness of the plate, L the distance of the counter supports,

and h the free-standing width of the Au wire.

The attenuation factor a is an important parameter. It has a large influence on the mechanical stability. A small factor provides higher immunity to external vibrations and more precise control on the size of the horizontal gap. To reduce the attenuation factor, we have used micro-fabricated break junction samples.

3.1.1 Micro-fabricated break junction samples

A micro-fabricated break junction sample reduces the free-standing width h by several orders of magnitudes compared with a conventional hand-made Au junction (i.e. from sub-mm to several hundred nm), which leads to very small attenuation factor [43].

A typical break junction sample used in this work is shown in Fig. 3.3. The Au structure is fabricated by e-beam lithography on a flexible spring steel plate substrate onto which a several μm thick insulating polyimide layer is cast, followed by the evaporation of a 10 nm thin adhesion layer of Ti under an angle of $\sim 50^\circ$ and the evaporation of 60 nm Au layer perpendicular to the sample. This procedure ensures good adhesion of the Au layer but avoids, due to the angle evaporation, Ti in the central region of the bridge. The bridge is typically 150 nm in width and 200 – 300 nm in length. The bridge is suspended by etching the polyimide in oxygen plasma. Further technical details of sample fabrication please see Appendix C.1.

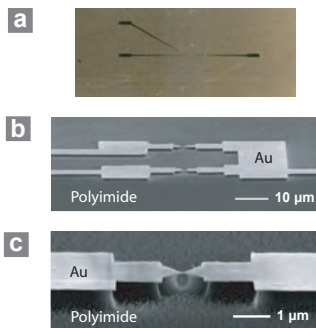


Figure 3.3: (a) Optical image of a typical break junction sample: Au structures are fabricated on an insulating polyimide covered steel substrate. The length of the sample is 24 mm; (b) An SEM image showing 2 junctions with 3 contacts at the center of sample; (c) Zoom-in picture of a freestanding Au bridge after plasma etching.

3.1.2 Discussion on the attenuation factor

We can estimate the theoretical attenuation factor based on the geometry and the size of our break junction sample according to eq. 3.1. With the thickness of the substrate $T = 0.3$ mm, the distance between the counter supports $L = 20$ mm and the length of the free standing bridge $h \approx 0.3$ μm , we get $a \approx 1 \cdot 10^{-6}$. However, in practice, the sample usually does not deform elastically. The plastic deformation of the sample results in an increase of attenuation factor a by approximately one order of magnitude [44].

Experimentally one can perform a calibration for attenuation factor (a_c) by measuring the variation of the tunneling current I with the gap separation d in vacuum [26; 45]. The expression for the tunneling current at low bias voltage through a square barrier of height Φ and thickness d is: $I \propto \exp(-2d\sqrt{2m\Phi}/\hbar)$, in which the horizontal separation d is related to the vertical movement of z by $d = a_c(z - z_0)$. If we use the measured slope of $\ln I$ as a function of z ($\ln I \propto -(2a\sqrt{2m\Phi}/\hbar)z$) and fix the work function of Au Φ_{vacuum} to the established value of 3.5 – 5.0 eV [46], we get $a_c = 1.6 - 4 \cdot 10^{-5}$ for the micro-fabricated break junction samples. This means that a vertical pushrod movement of 10 μm corresponds only to 2 – 7 Å separation of the two electrodes. These atomic contacts and the controllable sub nm-sized gap are ideal for single molecule measurements.

3.2 The setup

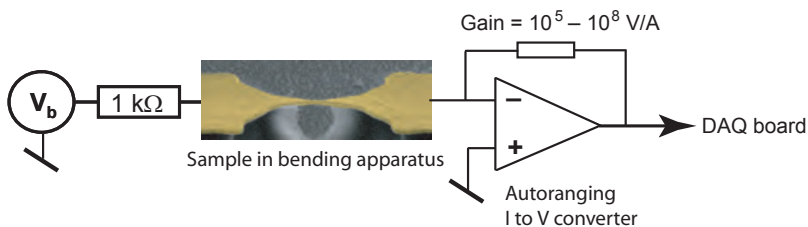


Figure 3.4: The basic circuit of the break junction setup consists of a voltage source, a series resistor, break junction sample in the 3 point bending apparatus and an autoranging IV-converter.

In our break junction setup, we use a bending apparatus to mount and bend the samples; a voltage source to apply a constant small bias voltage (max. 200 mV); and an I to V converter to detect the current flowing

through the Au bridge during its breaking process. It is important to have an autoranging *IV*-converter which can quickly change the gain over several decades because after breaking of the Au bridge, the tunneling current decays from mA to nA exponentially with respect to the tip separation. The circuit is completed by a series resistor (1 k Ω) to limit the maximum current and protect the original Au bridge (which has typical resistance of $\sim 200\ \Omega$). The data is recorded by a data acquisition board (DAQ) connected to a computer (Fig. 3.4). In order to measure organic molecules in a chemical environment, a liquid cell is added to the setup. These parts will be explained separately in the following pages.

3.2.1 The bending apparatus

To perform a break junction measurement, the sample is held by two counter supports on the side, positioned at a distance of 20 mm (Fig. 3.5 Sample holder). A push-rod is pressing at the center from below to bend the substrate. The pushrod is driven by a stepper motor (Phythron GLD), the movement is reduced by a planetary gear (reduction 1:4) and a worm gear (reduction 1:50). One full turn of the worm gear (= 200 motor turns) moves the push-rod 1 mm in vertical direction. The motor does 200 steps for one turn. Therefore one step corresponds to a movement of 25 nm (1/40000 mm). Because 1 step is electronically divided in 8 substeps, one substep corresponds to a vertical movement of 3.125 nm (1/320000 mm). The motor is controlled by a PC and the speed can be adjusted between 500 and 9999 substeps per second (1.56 – 31.2 $\mu\text{m/s}$). To fully open/close the break junction 10-20 motor rotations ($\sim 200 - 400\ \mu\text{m}$) are needed. Piezo actuators are not able to perform such long distances (typically max. $\sim 100\ \mu\text{m}$) and therefore it is not considered in our setup [26].

3.2.2 The liquid cell and electrical contacts

A liquid cell is gently pressed directly on the sample via a soft Viton tube (Fig. 3.5c). A tight contact of the cell to the sample surface is ensured via a spring (Fig. 3.5b). This allows the easy operation of organic molecules in the natural liquid environment. Moreover, it allows bubbling the cell with argon to keep an oxygen free environment. It is very important to keep molecules in the correct and stable state for *in situ* chemical reactions such as deprotection and electrochemistry.

To ensure good electrical contact during the bending of the break junction sample, the contacts are fixed to the pads with a clamp and an indium layer in between (Fig. 3.5c). With this structure, the contacts can also follow

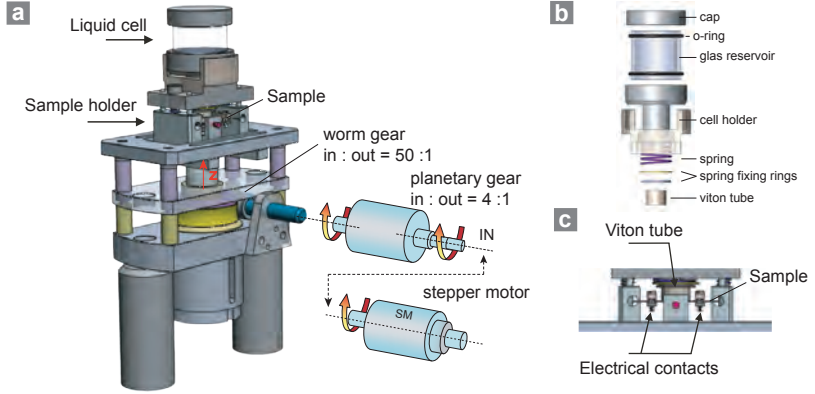


Figure 3.5: (a) The actual MCBJ setup composed of a liquid cell; a sample holder (with a sample inside); and a pushrod (red arrow) driven by a stepper motor. The movement of the stepper motor is reduced by a planetary gear and a worm gear; (b) Schematic of the liquid cell; (c) Zoom-in picture of the sample holder with a soft Viton tube through which the liquid cell is pressed directly on the sample and the electrical contacts of the break junction sample.

the bending movement of the sample, avoiding possible scratches during the bending process.

3.2.3 The autoranging I to V Converter

In break junction measurements, we apply a constant small bias voltage (max. 200 mV). The current flowing through the junction during an opening/closing cycle varies between μA - and pA -range. This current is measured by a custom-made autoranging low-noise current to voltage converter (AIVC) [47]. The converter implements a fast automatic switching of the gain between 10^5 and 10^8 V/A (recent version between 10^4 and 10^9 V/A) and enables measurements of conductance values ranging over many orders of magnitude, from the quantized conductance value above a single atom contact $G = G_0 = 2e^2/h$ down to $G \sim 10^{-7} G_0$.

To ensure low-noise performance the AIVC is subdivided into two separated well shielded aluminum boxes: the I to V converter (upper one) and the autoranging unit (bottom one) as shown in Fig. 3.6a.

The simplified block diagram of the AIVC is shown in Fig. 3.6b. The I to V converter in the first shielded box consists of a low-noise, precision and high-speed operational amplifier (OP) and a 4-channel CMOS analog

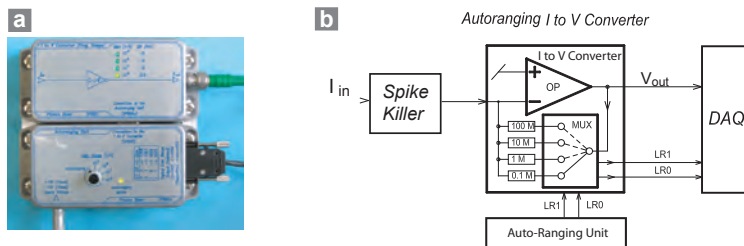


Figure 3.6: (a) Photo of the auto ranging I to V converter. (b) Schematics of the AIVC. The selected range is coded in a binary digital number ($LR1$ and $LR0$) and is sent to DAQ. The spike-killer suppresses the unwanted spikes occurring during range switching at the input of the AIVC.

multiplexer (MUX) which has four different feedback resistors (0.1 M Ω , 1 M Ω , 10 M Ω and 100 M Ω) which correspond to the four decades of gain: 10^5 , 10^6 , 10^7 and 10^8 V/A.

The auto-ranging unit is installed in the second shielded box. A 70 Hz low pass filter provides the arithmetic mean value of the rectified signal. A window comparator detects whether the mean value is smaller than 0.5 V (Low Level Threshold) or higher than 7.5 V (High Level Threshold). The corresponding signals are named “Too Low” or “Too High”. The automatic gain control logic switches to the next higher range when the signal “Too Low” is activated; similarly the next lower range is chosen when the signal “Too High” is active. The selected range is binary coded in the two signals $LR1$, $LR0$. These digital range signals are sent to the I to V converter to select the right feedback resistor as well as to the DAQ to record the gain.

Prior to the input of the AIVC, a spike-killer (SK) is mounted in order to reduce voltage spikes generated by the AIVC during switching between different gain ranges. On high impedance sources these spikes can reach levels of several volts. The spike-killer reduces the glitches typically by two orders of magnitude, therefore can protect the break junction sample during the opening and closing processes.

3.3 Combining electrochemistry and break junction

Electrochemistry studies the charge transfer between reactants and electrodes and therefore relates electrical and chemical effects. By applying a voltage to an electrode relative to a reference electrode, the chemical potential of the electrode can be altered. If the reactants are redox-active

molecules, they can move towards the surface of electrodes, adsorb and exchange electrons. As illustrated in Fig. 3.7, molecules turn into the oxidized state by giving electrons to the electrode. This happens when the chemical potential of the electrode is lower than the HOMO. Similarly, molecules turn into the reduced state by taking electrons from the electrode when the chemical potential is higher than the LUMO [5].

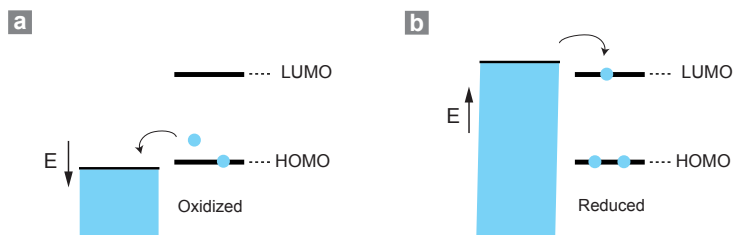


Figure 3.7: (a) A redox molecule is oxidized by losing one electron to the electrode when the chemical potential of the electrode is lower than the HOMO level of the molecule; (b) The molecule is reduced after taking one electron from the electrode when the chemical potential of the electrode is higher than the LUMO level of the molecule.

Combining electrochemistry and break junction measurements provides an opportunity to study the transport properties of redox molecules (connected by source and drain electrodes) whose oxidized and reduced states can then be tuned by adding a third electrode (reference electrode). We will describe the technical details in this section.

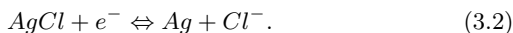
3.3.1 A brief introduction to 3-electrode electrochemical cell

In experimental electrochemistry, the 3-electrode cell is one of the most common configurations used to study electrochemical reactions. It consists of a working electrode (WE), a reference electrode (RE) and a counter electrode (CE). The WE is the electrode where the electrochemical reactions of interest take place and where the potential needs to be controlled precisely. The RE is used to maintain a constant potential relative to the potential of the standard hydrogen electrode (SHE) in the experiment. In order to maintain a stable potential, no current is allowed to pass through the reference electrode. To complete the cell we have to introduce a third electrode, the CE. A current is forced between WE and CE by a potentiostat, high enough and in proper polarity to keep the chemical potential of the working electrode at a preset value with respect to that of the reference electrode.

The 3 electrodes

1. **The working electrode (WE):** It is the electrode at which the reactions of interest take place. For many physical electrochemistry experiments, the WE is an inert material such as gold, platinum, or glassy carbon. Designs of working electrodes are diverse. Most commonly are small spheres, discs, short wires, evaporated thin films or single crystals of a metal. An essential feature is that the electrode should not react chemically with the solvent or the electrolyte.
2. **The reference electrode (RE):** In electrochemistry, the chemical potential must always be given relative to a known reference electrode. The essential role of the RE is to maintain a constant potential during measurement. All electrode potentials are measured vs. the standard hydrogen electrode (SHE: $Pt/H_2 \rightleftharpoons 2H^+$). This electrode couple is arbitrarily defined as zero volt. However, practically using this electrode is not at all easy. It requires a steady flow of hydrogen bubbling onto a platinum plate with large surface area.

A much easier way is to use an electrode couple that has a clearly defined potential relative to the SHE. A commonly employed system is a Ag/AgCl electrode. This electrode consists of a silver wire, coated with silver chloride, which is immersed in a solution containing 3M sodium chloride. A porous Vycor frit is used to form the ionic conducting channel between the reference electrode solution and the sample solution. The redox process for this electrode is:



The potential of this system is determined by the activity a_{Cl^-} of Cl^- ions in the solution from the Nernst equation:

$$E = E^0 + \frac{RT}{nF} \ln\left(\frac{1}{a_{Cl^-}}\right), \quad (3.3)$$

with E^0 the standard potential (the potential of the electrode at unit activity under standard conditions), R the universal gas constant ($= 8.314 \text{ J} \cdot \text{K}^{-1} \cdot \text{mol}^{-1}$), T the absolute temperature, F the Faraday constant ($= 9.648 \cdot 10^4 \text{ C} \cdot \text{mol}^{-1}$) and n the number of electrons transferred in the cell reaction.

It is generally more convenient to consider concentrations rather than activities ($a_{Cl^-} = \gamma_{Cl^-} \cdot [Cl^-]$), where γ is the activity coefficient. The redox potential E for the Ag/AgCl reference electrode with 3 M sodium chloride at 25 °C is 0.196 V (vs. SHE).

3. **The counter electrode (CE):** The CE is a conductor that completes the cell circuit. In lab cells it is normally an inert conductor like platinum or graphite. The CE often has a surface area much larger than that of the WE to ensure that the reactions occurring on the working electrode are not surface area limited by the counter electrode.

The potentiostat

A potentiostat is used to provide a constant potential drop between the WE and the RE. The principle is shown in Fig. 3.8 where the cell can be approximated by a very simple equivalent circuit. The electrolyte is characterized as solution resistance R_s and the interface of the electrode/electrolyte as electrical double layer capacitance and resistance in parallel (C_{dl} and R_e shown for the WE).

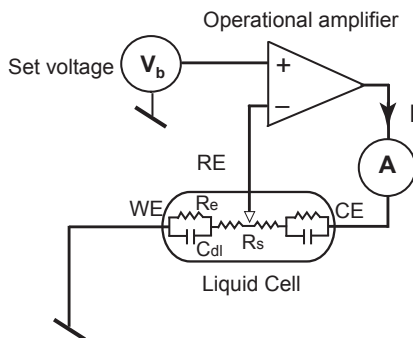


Figure 3.8: Simple potentiostat for maintaining a constant potential (V_b) difference between a reference electrode (RE) and a working electrode (WE); R_s is the resistance of the electrolyte; C_{dl} is the double layer capacitance and R_e is the resistance in parallel at the interface of WE/electrolyte.

It can be seen that the device is simply a bipolar operational amplifier (OPA). The WE is connected to the non-inverting input (+), the RE to the inverting input (-), and the counter electrode to the output. Considering the set voltage $V_b = 0$ V, the potential difference between WE and RE is amplified and inverted and output by the OPA. A matching current passes the electrolyte from the counter electrode to the working electrode. This polarizes the WE exactly so that the potential difference between the RE input and the WE input is set to be zero. If we want to shift the potential of the WE to a certain value referring to that of the RE, we could insert

a voltage V_b ($\neq 0$) to the non-inverting input (+) of the amplifier. In electrochemistry, one usually considers the potential of the RE as zero. The potential E at the WE/electrolyte interface therefore equals $-V_b$.

A high input-impedance operational amplifier is used in order to further diminish the current passing through the reference electrode. And the RE input is commonly protected by an input resistor, which prevents the potential amplifier from being destroyed by static high voltage shocks when the input is open.

An example of cyclic voltammetry

The 3-electrode electrochemical cell allows us to probe the mechanisms and kinetics of charge transfer process of a redox system in solution. Shown here is an example of cyclic voltammetry. This technique is ideally suited for a quick search of redox couples present in solution. A typical voltam-

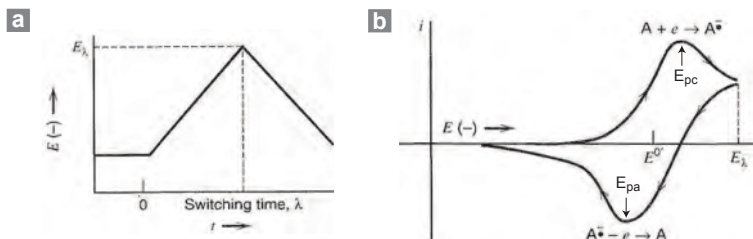


Figure 3.9: (a) Cyclic potential sweep; (b) Resulting cyclic voltammogram. [5]

mogram is shown in Fig. 3.9. E is the potential applied at the interface of WE/electrolyte referred to the potential of the reference electrode. It starts at $t = 0$ and up to some negative switching value, E_λ , at which the scan is reversed back to the starting potential (Fig. 3.9a). The cell current in Fig. 3.9b is observed to increase, indicating that the reduction of a redox compound A in the solution is taking place ($A + e \rightarrow A^{\bullet-}$). The current peaks at E_{pc} (with value i_{pc}) then drops due to depletion of the oxidizing species from diffusion. During the return scan the processes are reversed (oxidation is now occurring: $A^{\bullet-} - e \rightarrow A$) and a peak current at E_{pa} (with value i_{pa}) is also observed but with an opposite sign. Providing that the charge transfer reaction is reversible and the redox products are stable, the ratio of the reverse and the forward current peak values verifies $i_{pc}/i_{pa}=1$. The corresponding peak potentials E_{pc} and E_{pa} are independent of scan rate and concentration, so that $(E_{pc} + E_{pa})/2$ is a good approximation

of $E^{0'}$ which is the formal potential for the redox reaction. Furthermore, $E_p = E_{pa} - E_{pc}$ should be close to 59 mV for one electron transfer reaction at all scan rates. These features are very convenient diagnostic tools to test for the reversibility of a redox process and stability of the reaction products.

3.3.2 Combining a potentiostat with the break junction setup

Taking the advantage of a potentiostat that can maintain the potential of an electrode to a certain value referred to a reference electrode, the combination with our break junction setup provides us the possibility to study the charge transport through single molecules in their controlled redox states.

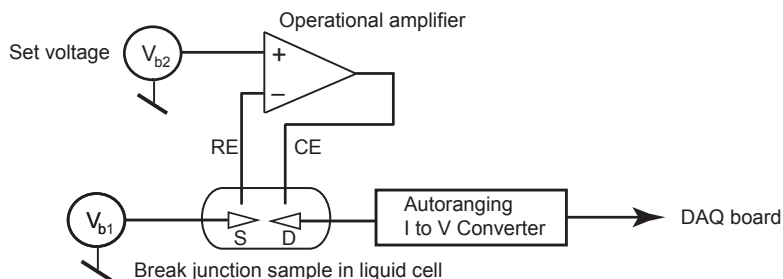


Figure 3.10: The circuit of the break junction setup combined with a potentiostat. Break junction source-and-drain electrodes serve as working electrodes. The current flowing in the cell is detected by the auto-ranging I to V converter.

The schematic of the circuit is shown in Fig. 3.10 where the break junction source-and-drain electrodes in the liquid cell serve as the working electrode.

In the experiments, a constant small bias voltage V_{b1} ($= 0.1$ V) is applied between the source/drain electrodes and the current in the cell is detected by the autoranging I to V converter. When the Au junction breaks open, this current is the sum of two contributions: (a) the tunneling current through single molecules due to applied bias voltage V_{b1} between source/drain electrodes, which is typically in the range of \sim nA; and (b) the electrochemical cell current between the CE and the source-and-drain electrodes where electron transfer occurs between bulk reactant and the whole surface of the electrodes with the applied potential V_{b2} . Depending on the area and reactant concentration, this current can easily be as large as μ A. In order to measure the signal of single molecules, it is required to reduce the electrochemical cell current. An efficient way is to protect the surface of Au

structures as we will see below.

3.3.3 Sample modification for electrochemical break junctions

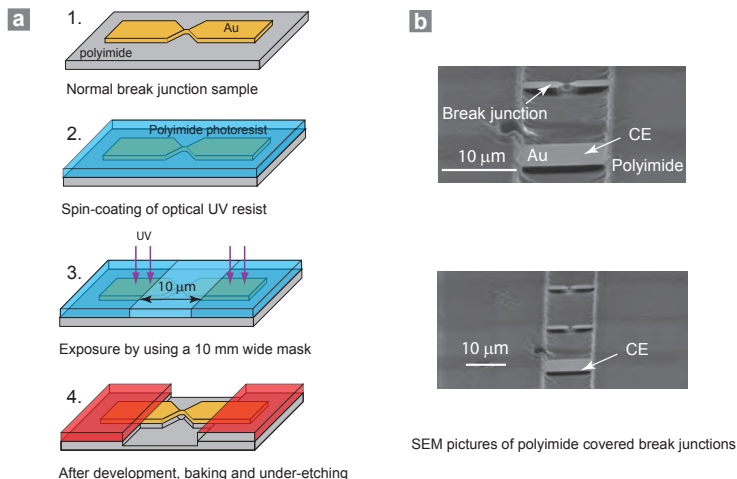


Figure 3.11: (a) Illustration of fabricating a polyimide covered junction with standard UV-lithography by using a stripe mask with 10 μm in width: step 1 - A normal break junction sample after metal deposition; step 2 - Spincoating of polyimide photoresist; step 3 - UV exposure with a stripe mask with 10 μm in width; step 4 - after development, baking and hardening of the polyimide resist, plasma etching makes a free-standing Au bridge. (b) SEM pictures of polyimide covered break junctions after plasma under-etching. A flat Au structure is fabricated close by as the counter electrode (see arrows).

We use polyimide photoresist (HD-4104, HD-microsystem) to cover the junction by standard photolithography as illustrated in Fig. 3.11a: Step 1 - It starts with a normal break junction sample with Au structures; Step 2 - Spincoating of polyimide photoresist (thickness: $\sim 3 \mu\text{m}$); Step 3 - UV exposure with a stripe mask with 10 μm in width; step 4 - after development, baking and hardening of the polyimide photoresist, plasma etching makes a free-standing Au bridge. SEM pictures of polyimide covered break junction samples are shown in Fig. 3.11a. The total area of Au structure exposed to liquid is $\sim 25 \mu\text{m}^2$, with the remaining Au surface being covered with polyimide. The hardened polyimide is resistant to polar organic solutions such

as dichloromethane and acetonitrile. A counter electrode is also fabricated on the same sample in this case. Using this structure and configuration, the electrochemical cell current can be reduced to the sub-nA range and it is therefore now possible to measure the signal of molecular junctions in an electrochemical cell.

Chapter 4

Statistical analysis: Seeing signals of molecular junctions

In our break junction setup we measure the conductance G of a suspended Au bridge during its breaking process controlled by vertical pushrod movement z . The Au junction is repeatedly opened and closed first in pure solvent and then in the solution of target molecules. We will see that conductance traces $G(z)$ show a significant difference between the two situations. Since single curves usually vary from each other, we need a proper statistical analysis in order to quantify the conductance value of a particular molecular junction. In this chapter we will introduce a histogram which is based on a logarithmic representation of G . Combining with conventional linear G -histogram, the molecular signals can easily be identified and deduced.

4.1 Breaking process in pure solvent

We first consider the junction breaking process in a pure solvent (mixture of THF/Mesitylene = 1:4 v/v-ratio). Fig. 4.1 shows three typical conductance traces with several breaking features. The original junction with ~ 150 nm in width and $200 - 300$ nm in length has a conductance value well above G_0 . When the substrate is bent, the Au bridge is stretched and $G(z)$ decreases. When the bridge enters in the range of several strands of Au atom chains, the decrease evolves in conductance plateaus for G values above the quantum conductance unit G_0 (as illustrated in step **1**). This process is clearly seen in the linear plot (Fig. 4.1a). There is a so-called “last plateau”, whose value is $G \approx G_0$ (see arrows, step **2**). This last plateau corresponds to a single atom Au contact as explain in the Section 2.2. If the junction is elongated further, it breaks open.

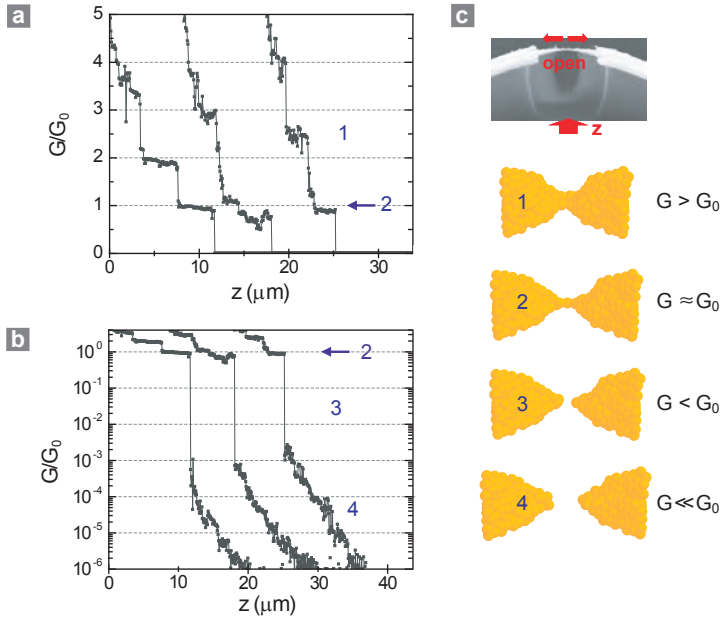


Figure 4.1: Three typical opening curves measured in pure solvent and schematics of breaking process. In break junction experiments, the pushrod is driven at a velocity of $v_z = 30 \mu\text{m/s}$, so that the two Au leads separate at $0.5 - 2.0 \text{ nm/s}$. The curves are shifted horizontally for clarity: (a) $G(z)$ plot with conductance plateaus at multiple values of quantum unit G_0 ; (b) $\log G(z)$ presentation with the full view of breaking process; (c) The breaking features are illustrated in several steps: step **1** - quantized conductance plateaus; step **2** - the “last plateau” of single Au atom at G_0 ; step **3** - breaking open of the junction; step **4** - stabilization of the electrodes.

A $\log G(z)$ curve gives the full overview of the breaking process between several G_0 and $10^{-6} G_0$ (Fig. 4.1b). After the formation of a single atom Au contact at G_0 , a sudden decrease of G is evident in the $\log G(z)$ curves (step **3**). This is thought to be caused by a sudden contraction and rearrangement of the Au atoms, reshaping the front end of the two Au electrodes. The down-jump typically stops at a value of $G \approx 10^{-3} G_0$, when electron tunneling between the electrodes sets in (step **4**). The tunneling current decays exponentially with gap distance d , whereas on a $\log G$ vs $\ln z$ plot, it decays linearly.

4.2 Wiring molecules

When molecules with terminal anchor groups are added in the solution, the situation changes markedly. Anchor groups such as thiols (-SH) form covalent bonds with Au atoms, therefore a single molecule can be wired between two atomic contacts during breaking open of the Au bridge. Because the covalent Au-S bond is stronger than a Au-Au bond [48; 49], the gold atoms migrate to the ends of the contacts to form elongated tips when the electrodes are pulled apart (red arrows in Fig. 4.2a) This process continues until the force exceeds the strength of the Au-Au bond and the molecular junction breaks open. By measuring the electrical conductance G during this process, we can anticipate that G will stay approximately constant as the electrodes are pulled apart during stretching, but it drops suddenly when the molecular junction breaks open.

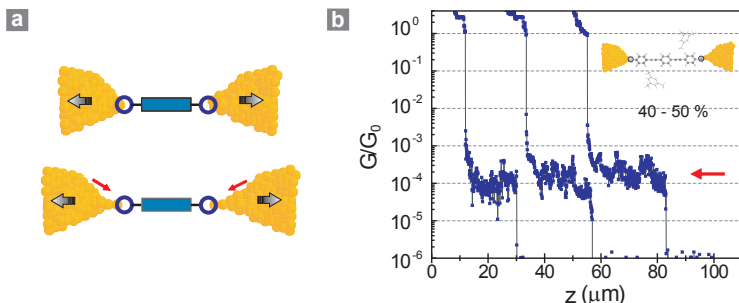


Figure 4.2: The breaking process in solution of OPE-dithiol molecules after *in situ* removing of the acetyl protection groups: (a) Schematics of formation of a molecular junction: A single molecule is anchored to electrodes through terminal Au-S bonds. While the electrodes move apart, Au atoms are pulled by the anchored molecule to form elongated tips (red arrows); (b) Three typical single $\log G(z)$ curves show clear noisy plateaus at $\approx 10^{-4} G_0$.

We take an oligo-phenylene ethynylene (OPE) molecule with acetyl-protected thiol anchor groups as an example. To assess the conductance G of the molecule, the junction is periodically opened and closed in the presence of 0.25 mM solution of molecules in a 3 mL mixture of THF/Mesitylene (1:4 v/v-ratio) to which 30 μM tetrabutylammonium hydroxide (TBAH) was added to remove the acetyl protection groups *in situ*. The TBAH concentration for a proper deprotection was established via thin layer chromatography (TLC). Upon deprotection the molecular solution changes color from transparent blue to bright yellow. During the measurements, the solution was

kept under Ar atmosphere to prevent the deprotected bifunctional molecules from polymerization via disulfide bond formation. Further details of deprotection process are described in Appendix C.2.

Three $G(z)$ curves with the OPE-dithiol molecules are shown in (Fig. 4.2b). Instead of a sudden drop followed by a tunneling slope, as it is observed in the solvent when the junction opens, clear conductance plateaus appear at G values below G_0 , typically at $G \approx 10^{-4} G_0$ in this case. This is the signature of the formation of a molecular junction. When the molecular junction breaks open, there is another sudden drop of conductance value. The chance of forming molecular junction is not unity, but amounts to a reasonably large fraction of 40 – 50 % in this case. In the other cases, the electrodes do not catch molecules. These curves show similar tunneling decay behavior as shown in pure solvent (see Fig. 4.1b).

4.3 Statistical histograms: the linear and logarithmic representations

Since the single conductance curves vary from each other and there are fluctuations in the signal, it is important to implement a statistical analysis in order to overcome junction-to-junction variations and quantify conductance value of a particular molecular junction. A conductance histogram was first proposed and implemented in atomic junctions [6; 50; 51]. It has subsequently also been used in molecular junctions [52; 40; 25]. Peaks in the histogram point to preferred junction geometries. Evidence for the formation of few-molecules junctions was derived from the observation of a series of G values appearing at multiples of a fundamental single molecule value. But because not all the curves show clear molecular plateaus, data selection schemes have been applied in order to highlight the molecular signature [53; 54; 55; 56; 57].

We introduce here an alternative histogram based on the logarithm of G . We take all data, and only subtract a background that is adapted to the physics of the problem.

We first take 100 consecutive opening conductance traces $G(z)$ of OPE-dithiol molecules and determine the probability with which a particular G -value is measured, $p_G(G)$. This is depicted in the conductance histograms of Fig. 4.3a (blue histogram). There is a distinct peak appearing at around $1 \cdot 10^{-4} G_0$, however, the signal is masked by a strong background.

We notice that the background comes from the tunneling decay. Since there is $\sim 50\%$ chance that the electrodes do not catch the molecule, the exponential decay of tunneling current must also contribute to the conductance histogram, as already seen in the case of pure solvent Fig. 4.3a (grey

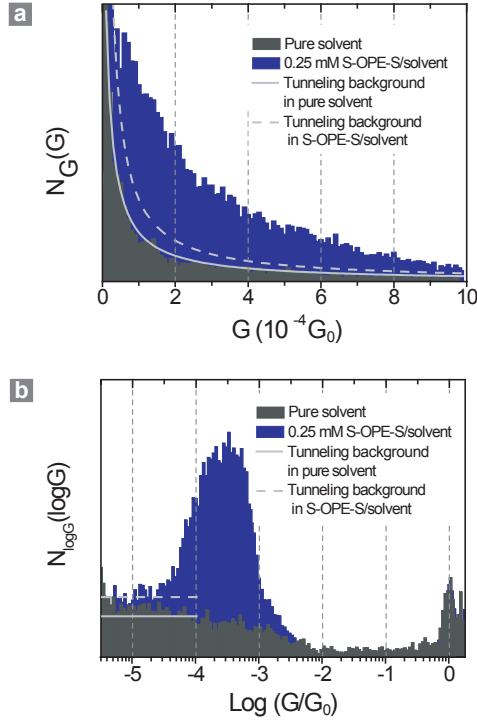


Figure 4.3: Two presentations of histograms with indication of tunneling background (solid lines for pure solvent and dash lines for the case of OPE-dithiol): (a) In the linear histogram $N_G(G)$ (bin size: $\Delta G = 1 \cdot 10^{-5} G_0$), tunneling background is $1/G$ dependent. Whereas a distinct peaks appearing at around $\approx 10^{-4} G_0$ for OPE-dithiols, however, the signal is masked by a strong background; (b) In the logarithmic histogram $N_{\log G}(\log G)$ (bin size: $\Delta G = 4 \cdot 10^{-2} G_0$), tunneling background shows a constant value in both case. In contrast with pure solvent, a pronounced peak appears for OPE-dithiol, indicating the signal of molecular junctions.

histogram) whereas $p_G(G)$ decays smoothly (grey line).

Tunneling physics tells us that conductance G is exponentially dependent on the gap distance d , i.e., $G \propto \exp(-2\kappa d)$. Here, $\kappa = \sqrt{2m\phi}/\hbar$ is the decay constant, ϕ the apparent barrier height, and m the electron mass. Furthermore, $d = a(z - z_0)$, where a is the attenuation factor of the MCBJ [26; 44], and z_0 is defined as $z(d = 0)$. Rewriting this, we find $\ln G = -2\kappa a z + \text{const.}$

It seems therefore much more appropriate to plot histograms of $\ln G$ rather than of G .

Making use of this expression, we can now calculate the expected tunneling contribution in the conductance histograms. If we denote with p_G , $p_{\ln G}$, and p_z the respective probabilities of measuring a certain value of G , $\ln G$ and z , we may write

$$p_G(G) dG = p_{\ln G}(\ln G) d\ln G = -p_z(z) dz. \quad (4.1)$$

Here, $p_z(z) = R/v_z$, where R is the data acquisition rate, and v_z is the velocity of the vertical push-rod. In our case, both these quantities are constant: $R = 500$ points/s, $v_z = 30$ $\mu\text{m/s}$. Solving eq. 4.1 for $p_{\ln G}$ yields

$$p_{\ln G}(\ln G) = \frac{R}{2 v_z \kappa a}. \quad (4.2)$$

Consequently, $p_{\ln G}$ is constant, whenever ϕ and a are constants. Hence, in a $\ln G$ - or $\log G$ -histogram, tunneling shows up as a constant background. In Fig. 4.3(b), we show a $\log G$ -histogram built from the data in Fig. 4.3(a). A constant background is indeed present for $G \lesssim 1 \cdot 10^{-3} G_0$ for the pure solvent (solid light gray line), for which tunneling is the only expected contribution. In contrast, clear peaks appear in the presence of OPE-dithiol. The $\log G$ -histogram representation is very powerful for another reason: it presents a full overview of the data. At a glance, both the single-atom Au contact peaks ($G \approx G_0$) and the molecules signal ($G < 10^{-3} G_0$) are seen. Between 10^{-2} – $10^{-3} G_0$ (depending on the sample) and G_0 , there is almost no weight in the histograms. This indicates that the Au atoms retract quickly immediately after breaking the gold atom bridge, as was already shown in Fig. 4.1 (step **3**).

The tunneling background, which is constant in a $\log G$ -histogram, is inversely proportional to G in a G -histogram. Solving eq. 4.1 for p_G yields

$$p_G(G) = \frac{R}{2 v_z \kappa a} \frac{1}{G}. \quad (4.3)$$

As can be seen in Fig. 4.3a, this expression perfectly matches the G -histogram of the pure solvent. The solid light gray line backgrounds of Fig. 4.3a and b correspond to the same $R/(2 v_z \kappa a)$. Similarly we can use this property to indicate the tunneling background for the histograms on OPE-dithiol molecules as marked by dash light gray line.

4.4 Deducing the conductance value of molecular junctions

Since tunneling contribution shows up as constant background in $\log G$ -histogram, it can then be subtracted easily. We now focus on the molecular signal and try to deduce the conductance value of a single molecular junction.

After subtracting the tunneling background of the histogram (defined by the constant value to the left of the molecular peak), we fit the remaining molecular signal peak with a Gaussian function. This procedure is highlighted with the curves in Fig. 4.4a). To determine the center value, we need to transform this Gauss function from the logarithmic to the linear representation.

The conversion from the $\log G$ -histogram, $N_{\log G}(\log G)$, to the linear one, $N_G(G)$, is given by:

$$N_G(G) = N_g(g) \frac{\log(e)}{G} \frac{\Delta G}{\Delta g}, \quad (4.4)$$

where ΔG and Δg denote the (constant) bin-size in the G - and $\log G$ -histogram, respectively.

The Gaussian fitting of molecular signal in the $\log G$ -histogram is expressed as:

$$N_g(g) = C \exp \left(-(g - g_c)^2 / 2w_g^2 \right), \quad (4.5)$$

where w_g denotes the width, g_c the center value, and C a constant. This Gauss function is transformed into the linear G -histogram, using eq. 4.4:

$$N_G(G) \propto \frac{\exp \left(-(\log G - g_c)^2 / 2w_g^2 \right)}{G}. \quad (4.6)$$

This transformation is explicitly illustrated in Fig. 4.4. The gross molecular signal, which appears as a relatively wide Gaussian-like peak in the $\log G$ -histogram is converted into a highly asymmetric peak in the linear histogram. The low conductance side of the peak is compressed to values close to zero, leading to a sharp increase on the left, whereas the high conductance side is stretched into a long tail with approximate $1/G$ dependence. From the peak value G_c we deduce the conductance of an OPE-dithiol junction is $G_{\text{OPEdithiol}} = 1.2 \cdot 10^{-4} G_0$. There seems to be only one broad molecular peak in G -histogram in this case. We can also fit this broad peak by multiple Gaussian peaks where the conductance value of a single molecular junction is defined by the first Gaussian peak. The two methods give similar

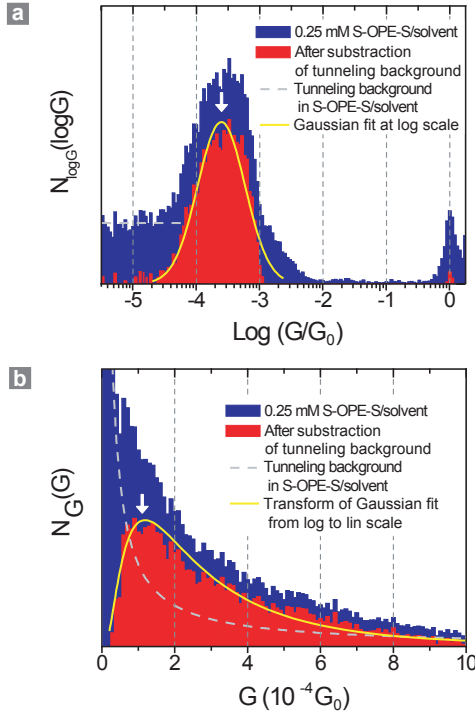


Figure 4.4: (a) Subtraction of tunneling background (defined by the constant value to the left of the molecular peak as marked by a dash line) and Gaussian fit of remaining peak in $\log G$ -histogram and (b) Subtraction of tunneling background in corresponding G -histogram. By transferring the Gaussian fit from log-scale to lin-scale (yellow lines), it is deduced from the peak value (see arrow) that the conductance of an OPE-dithiol junction is $G_{OPE-dithiol} = 1.2 \cdot 10^{-4} G_0$.

values [58]. We stress that the peaks are centered at a different position in the two kinds of histograms. The peak appears at slightly lower values in the G -histogram compared to the $\log G$ one.

4.5 Sample-to-sample variation

After describing the fitting and analysis procedure, we can discuss the sample dependent variances of measurements in the $\log G$ -histogram.

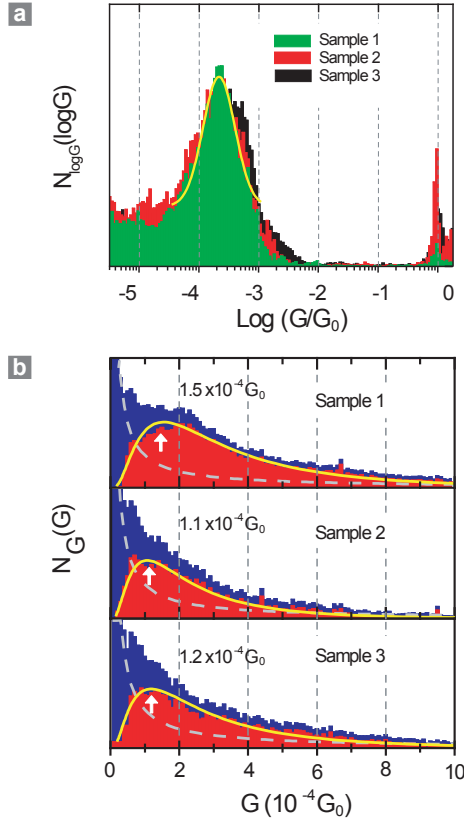


Figure 4.5: Three OPE-dithiol measurements of different break junction samples showing the repetition and reliability: (a) Overlap of $\log G$ -histograms; (b) G histograms after background subtraction and transformation of Gaussian fitting from log-scale to lin-scale. The peak values are also marked.

Fig. 4.5 shows three histograms for OPE-dithiol built each from 100 conductance traces from three distinct samples. All three histograms agree with each other very well. Following the method described above, we make

Gaussian fit in the $\log G$ histograms as shown in Fig. 4.5a (only the fitting for the front histogram is shown for clarity) and obtain the peak value g_c and the width w . We then use the transformation between the log- and lin-scale histograms to deduce the conductance values G_c in the linear scale. The values for g_c , w and G_c are summarized in Table 4.1.

Sample	g_c	w_g	G_c
	$\log(G_0)$	$\log(G_0)$	$10^{-4} G_0$
Sample 1	-3.67	0.54	1.5
Sample 2	-3.70	0.70	1.1
Sample 3	-3.60	0.75	1.2

Table 4.1: Values of g_c , w obtained from $\log G$ -histograms in Fig. 4.5a and G_c from G -histograms in Fig. 4.5b are quite similar for three different samples.

The transformation gives similar values in G -histograms. By taking the 3 conductance value and make standard deviation out of them, we find the conductance value of a OPEdithiol molecular junction which is $G_{OPEdithol} = (1.3 \pm 0.2) \cdot 10^{-4} G_0$.

4.6 Conclusion

We have put forward a new method to analyze conductance values G based on a histogram of the logarithm of G . The $\log G$ representation allows a simple background subtraction and provides an overview from the single Au atom contact to tunneling. Moreover, the single (few) molecule conductance values show up in a much more striking manner. In such a histogram all the weight that can be assigned to the presence of molecules anchoring in the gap yields a symmetric peak, whereas the data in a linear G representation is a strongly asymmetric peak that assumes a power-law dependence over almost the whole range of G -values, closely following $1/G$. In addition, we conclude that the features appearing in the conductance histograms obtained with break junctions (in MCBJ or STM configuration) are robust and can be realistically attributed to the molecular signature in these junctions.

Chapter 5

The role of contacts in molecular conductance

In order to wire molecules between source and drain electrodes and measure their transport properties, it is required to design molecules with anchor groups. Anchor groups not only ensure a mechanical stabilization of molecular junctions, but more importantly, provide at the same time electronic coupling between a molecule and the contact electrodes. Here we use oligophenylene ethynylene (OPE) molecules as model system. In the first section we compare binding properties of thiol and pyridine by systematically changing the linker groups. In the second section, more linker groups such as amines and different effects of side groups on thiol and amine anchored OPE molecules are discussed.

5.1 A comparison between thiol and pyridine

To date, thiols are the most widely used anchor groups to Au electrodes. They bind through the formation of Au-S covalent bond. Based on the knowledge of self-assembled monolayers (SAM), many electron donors, such as pyridines, can also have interactions with the Au surface through weak electron donor-acceptor bond. We study and compare here the effects of thiol- and pyridine- anchor groups on molecular conductance.

Fig. 5.1 shows the molecules designed in this work. Linker groups are changed gradually as marked by dash circles: With the same OPE conjugated backbone structure, OPE-dithiol serves as a reference molecule (OPE_{SS}), then one thiol linker group is replaced by a pyridine nitrogen (OPE_{SN}), and finally we measure a symmetric OPE-bipyridine molecule (OPE_{NN}).

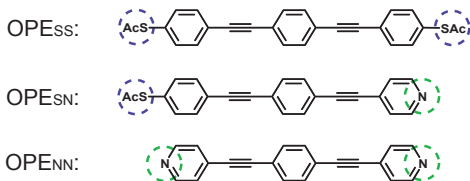


Figure 5.1: Structures of the molecules examined in this work. Linker groups are changed gradually as marked by dash circles: OPE_{SS}, OPE_{SN} and OPE_{NN}.

5.1.1 Molecular conductances of OPEs with thiol and pyridine anchors

As described in Section 4.2, the junction is opened and closed repeatedly in the 0.25 mM THF/mesitylene (= 1:4 v/v-ratio) molecular solution. In the case of thiol linker groups, an *in situ* deprotection is used to remove the acetyl group and obtain free thiols under Ar bubbling. For symmetric pyridine linkers, the junction is measured directly in the 0.25 mM molecular solution.

In all three cases, conductance traces of $\log G(z)$ show clear plateaus at G values below G_0 (Fig. 5.2a) and the formation probability of molecular plateaus are similar (40 – 50 %). Taking many curves, the plateaus build up a broad and pronounced peak in $\log G$ histograms (Fig. 5.2b). By fitting a Gaussian function on the overall peak and transform it back to the G -linear representation [58; 59], we deduce the single-molecule conductance value as shown in Table 5.1.

Molecule	No. of samples	G (G_0)	Length (Å)	w^b in $\log G$ histogram
OPE _{SS}	4	$(1.2 \pm 0.1) \cdot 10^{-4}$	20.7 (S,S)	0.72 ± 0.04
OPE _{SN}	3	$(5.7 \pm 2.4) \cdot 10^{-5}$	18.7 (S,N)	0.60 ± 0.08
OPE _{NN}	4	$(3.5 \pm 1.2) \cdot 10^{-6}$	16.6 (N,N)	0.74 ± 0.08

Table 5.1: Average single-molecule conductance values G for molecules examined, obtained by transforming the Gaussian fit in $\log G$ -histogram back to the G -linear representation. In addition, the full-width at half maximum w^b of the Gaussian peaks in $\log G$ -histograms is given as an indication of fluctuations of molecular signals. The length of each molecule is obtained after energy minimization using the MM2 force field (ChemDraw 3D).

All the three molecular signals in $\log G$ histograms show comparable width

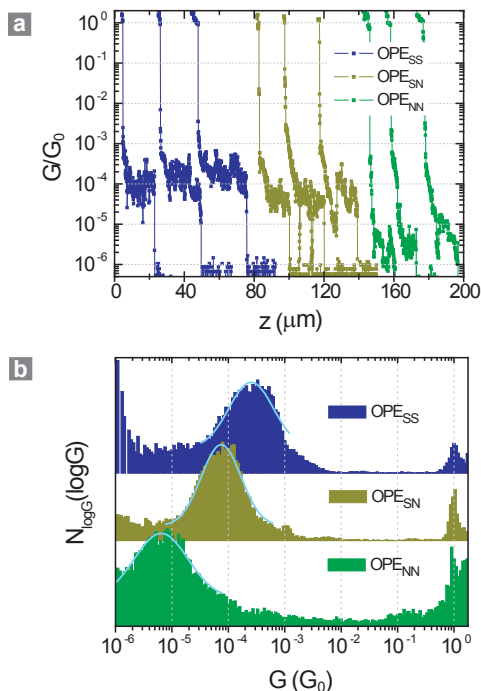


Figure 5.2: (a) Typical measurements of individual conductance traces $G(z)$ as a function of pushrod movement z during opening cycles in solution of OPEs with different linker groups; (b) Comparison of $\log G$ -histograms of measured conductance values $\log G(z)$ obtained for one hundred successive open cycles. The pronounced Gaussian-like peaks (solid fitting lines) in the histograms represent the signatures of the specific molecule investigated. The molecular junction conductance is deduced from the conductance peak G_{peak} .

and height. The striking effect is on the conductance values. By gradually changing thiol linkers to pyridine nitrogen linkers, the molecules become shorter, one would then expect that the conductance values increase. However the experiments show an opposite way: by replacing one thiol linker group of the OPE-dithiol (OPE_{SS}) with a pyridine nitrogen, conductance of a OPE_{SN} junction decreases to be half value. In the case of symmetric OPE_{NN} , it decreases further to be nearly two orders of magnitude lower than that of the OPE-dithiol. Our data shows that the contacts play an impor-

tant role in the electron transport of a molecular junction. We next discuss the conductance values based on tunneling physics and binding chemistry.

5.1.2 Discussion based on tunneling physics and binding chemistry

According to the theory of electron tunneling through an effective medium with distance d (here, molecule length), the conductance G is given by $G = A_{left} \cdot A_{right} \cdot e^{-\beta d}$. The decay constant β is determined by electronic parameters of the effective medium (here, the OPE backbone structure). For a given electrode material (here, Au), the prefactor A_{left} and A_{right} depends on the electron density-of-states at the point where the molecule contacts the left and right Au electrodes. For a simple estimation, we assume the prefactor A to be independent of the decay constant β . A is considered as “contact conductance” [60; 61]. For the decay constant β ($= 0.3 \text{ \AA}^{-1}$) of conjugated molecules, the length of molecules S-S, S-N, N-N as shown in Table 5.1 and the measured conductance values, we could calculate the “contact conductance” of A_S and A_N from any two molecules among them and check the validity for the third case. For example, taking the conductance values of symmetric OPE_{SS} and OPE_{NN} junction:

$$G_{SS} = A_S^2 \cdot e^{-\beta d_{SS}} \quad (5.1)$$

$$G_{NN} = A_N^2 \cdot e^{-\beta d_{NN}} \quad (5.2)$$

we can calculate the contact conductance of thiol: $A_S = 0.24 G_0$; and pyridine nitrogen: $A_N = 0.028 G_0$. In the term of “contact resistance”, the corresponding values are: $R_S = 54 \text{ k}\Omega$ and $R_N = 460 \text{ k}\Omega$, which are close to literature values of thiol and amine anchor groups [60; 61].

Doing similar calculation on the asymmetric OPE_{SN} molecule ($G_{SN} = A_S \cdot A_N \cdot e^{-\beta d_{SN}}$) based on measured conductance value, we obtain the contact conductance $A_S \cdot A_N = 0.019 G_0$. Quite interestingly, this value is not simply equal to the product of A_S and A_N which we have calculated from eq. 5.1 and eq. 5.2 but rather shows 3 times higher, indicating the electron transport is dominated by thiol anchors. Our data suggests that the assumption of an independent “contact conductance” does not hold. The disagreement may come from either the effects of anchor groups on the HOMO-LUMO gap of molecules or the location of molecular HOMO/LUMO levels relative to the fermi level of the electrodes. Since UV-vis spectra of the three molecules show small difference (see Appendix B.1), we think it is more probable that the contact properties affect the alignment of LUMO and HOMO levels regarding to E_F of electrodes.

It is generally accepted that thiol forms strong covalent bond with Au

($\text{RSH} + \text{Au} = \text{RS} - \text{Au} + 1/2\text{H}_2$) by taking one electron from it, and therefore the sulfur atom is electronegatively charged; In contrast, for a pyridine, the nitrogen forms weak coordination with gold with the tendency of losing its lone pair of electrons (electron donor) to Au atoms, therefore it is slightly electropositive. This effect moves the LUMO/HOMO states of OPE-bipyridine down relative to E_F . It has been described in literature (experiment [62] and theory [63]) that the dominant frontier orbital for transport is the HOMO level. We hence propose that the low conductance value of an OPE molecule with pyridine linkers is due to its large gap between HOMO and E_F level. This is supported by recent DFT/B3LYP calculations that HOMO level of an alkane-dithiol is closer to E_F ($E_{\text{HOMO dithiol}} - E_F \simeq 2$ eV) whereas an alkane-diamine is further away ($E_{\text{HOMO diamine}} - E_F \simeq 3$ eV) although the HOMO-LUMO gap is quite similar ($\simeq 8$ eV) [63]. For the asymmetric OPE_{SN} molecule, the HOMO level seems to be pinned by the coupling of thiol to Au. This would explain why its conductance value is only 2 times lower than in OPE_{SS} but an order of magnitude higher than in OPE_{NN} . Schematics of the band alignment of the three molecules are illustrated in Fig. 5.3.

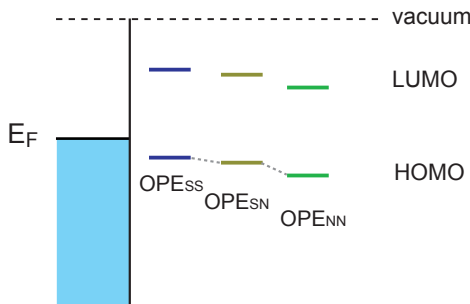


Figure 5.3: We propose to explain our experimental finding by band alignment of OPE molecules with different anchor groups. The HOMO level of a dithiol molecule is closest to E_F and that of a bipyridine molecule is further away. For an asymmetric thiol-pyridine molecule, the alignment of the HOMO level is dominated by the thiol linker.

In addition, we found that the full-width at half maximum w^b of the Gaussian molecular signal peak in the $\log G$ -histogram is quite comparable for all three anchored molecules. The peak width reflects the fluctuations in the molecular junctions which can be caused by, for example, the different orientations of phenyl-rings in molecular backbone structure which can

disturb the π -system; They can also come from the binding properties, as in the case of Au-S bond, from the switching between different binding sites (hollow, on-top, or bridge site). In the case of pyridine linker, the noise may be due to the sliding of pyridine atom, possibly also with different binding sites on the Au surface.

5.1.3 Concluding comments

In conclusion, we have systematically studied and compared the binding properties of thiol and pyridine nitrogen groups. We observed clear molecular signals in both symmetric and asymmetric structures. Comparison of the conductance values for different binding moieties indicates that the band alignment of LUMO and HOMO levels is crucial for the understanding of conductance values of formed molecular junctions. To further study this effect, we propose systematic I - V measurements on these molecules. In addition, we have found comparable binding fluctuations for OPE molecules with thiol and pyridine linker groups.

5.2 Side group effects

Amine ($-\text{NH}_2$) with an electron lone pair on nitrogen atom is another candidate for electron-donor anchor groups [64]. We also tested its binding properties. Molecules with amine anchor groups are shown in Fig. 5.4a with only OPE backbone (molecule **1a**) and to which two methoxy side groups are attached (molecule **1b**). OPE with methoxy anchor groups (molecule **2**) serves as a control. As comparison, the same structures but with dithiol anchor groups are also shown (molecule **3a** and **3b**.)

5.2.1 Conductance histograms and discussion

Fig. 5.4b shows typical $\log G$ histograms of the molecules. We first take look at the typical measurement of OPE-diamines (molecule **1a**). At first glance, an OPE-diamine molecule does not show clear molecular signal (as marked by dash line). We have measured for 11 samples with different concentrations and in different solvents (for more histograms see Appendix B.1) but all of them show similar results.

As both are nitrogen linkers, why does OPE-bypiridine show clear molecular signal but OPE-diamine does not? We propose to interpret our data by the orbital structure of the molecules. As shown in Fig. 5.5a, the aromatic π -system of pyridine is the same as that of benzene. The electron lone pair on nitrogen is contained in an sp^2 -orbital and is orthogonal to the π -system. In contrast, in aromatic amine (aniline in Fig. 5.5b), the sp^2 -hybridization

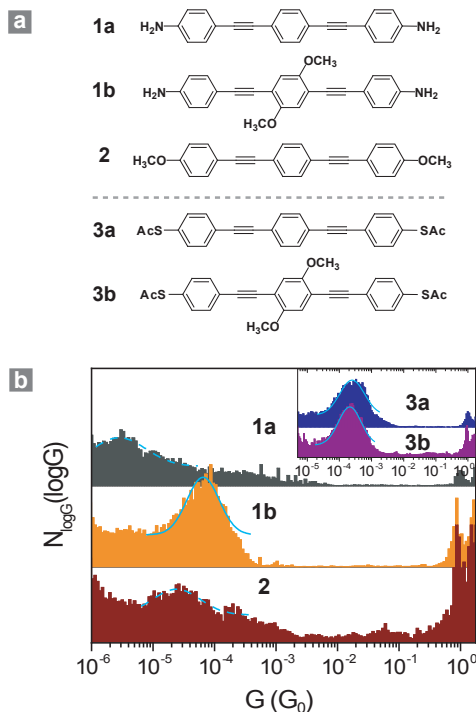


Figure 5.4: (a) OPE molecules with different anchor groups and with/without methoxy substitutes. (b) $\log G$ histograms of OPE-diamine (molecule **1a**) and OPE-diamine with side group (molecule **1b**). Molecule **1a** does not show clear molecular signal (marked with dash line) but molecule **1b** shows a surprisingly clear peak. OPE with methoxy anchor groups (molecule **2**) serves as a control. Inset: $\log G$ histograms of OPE-dithiol (molecule **3a**) and OPE-dithiol with side groups (molecule **3b**).

of nitrogen produces the optimal geometry for the overlap of its lone pair of electrons in a p -orbital with the aromatic array of p -orbitals on carbons in the ring. Due to the delocalization of the nitrogen lone electron pair with the rest of the aromatic π -electrons, the nitrogen here behaves as a π -electron donor to the phenyl ring (see arrows) [65]. Compared with pyridine, the binding of amines with gold is weakened and therefore does not show clear molecular signal.

Surprisingly, with the same anchors, a dimethoxy ($-\text{OCH}_3$) substituted

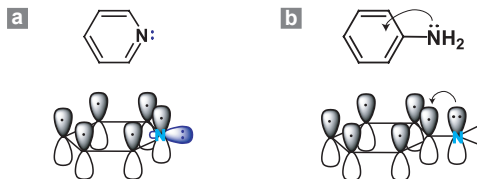


Figure 5.5: 3D representation of orbital interactions in: (a) pyridine, where six overlapping p orbitals (gray) comprise the aromatic six-electron π -system, and an sp^2 -hybrid orbital (blue) containing an electron lone pair is orthogonal to the π system; and (b) aniline, where the electron lone pair in p orbital of nitrogen atom overlaps with the π -system of the aromatic ring, behaving as a π -electron donor.

OPE-diamine (molecule **1b**) turns out to show a well-defined peak in histogram. Does the signal come from the effect of side groups on the binding property of amine anchors or other possible binding sites in the molecule such as dimethoxy groups?

We have carried out a control experiment with OPE-dimethoxy (molecule **2**). As there is no well defined molecular signal in histogram (marked by dash line), we therefore think the clear molecular signal of substituted OPE-diamine (molecule **1b**) still comes from the linking of terminal amines.

Using the same concept, we next discuss the effect of methoxy groups on the binding property of amines. There are two electron lone pairs in an oxygen atom. One pair of them is delocalized with the phenyl-ring π -system as the same effect in aromatic amine (Fig. 5.5b), behaving as well as a π -electron donor. Because the amine anchor groups are also in the same extended π -system, substituted dimethoxy can then strengthen the binding properties of amines to the Au surface, which makes the molecular signal well defined. The electron-donating methoxy also tend to shift the HOMO level closer to E_F level of the electrodes, as a result, proving higher conductance value of substituted OPE-diamine.

We have measured the similar molecular structures (molecule **3a** and **3b**) but with thiol anchor groups [58], where the same dimethoxy side groups basically show no effect on molecular conductance (inset of Fig. 5.4b). The contrast suggests that the side group effect on molecular conductance can strongly depend on the properties of anchor groups. Possibly a thiol anchor group binds to the gold strongly. As a result, it pins the molecular orbitals relative to the Fermi energy E_F of electrode. In the case of aromatic amine, because of the weak binding, the side groups affect the binding properties more efficiently.

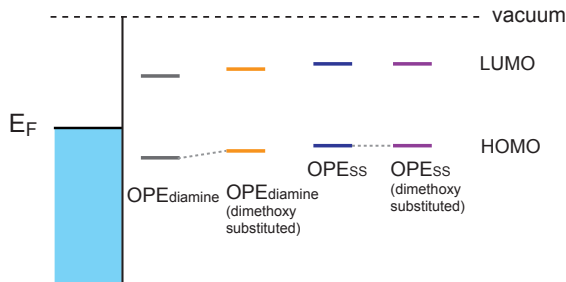


Figure 5.6: We propose the band alignment of OPE molecules with thiol and amine anchors under the effect of dimethoxy substituted groups. For a weak bond as Au-NH₂, the electron-donating side groups tend to shift the HOMO level closer to E_F level of the electrodes. While for a strong bond as Au-S, the electron transport is dominated by contact property and the side groups have no effect.

5.2.2 Concluding comments

In summary, we have compared the molecular signatures of amine- and thiol-anchored OPE molecules with and without the electron-donating side groups. Our data suggests that the effect of side groups strongly relates to binding properties of anchor groups. For a strong covalent bond such as Au-S, the contact property may dominate the transport property, while for a weak donor-acceptor bond, side groups play a more effective role. These preliminary results motivate more molecular design and experimental work to understand the relationship between properties of substituted groups and anchor groups. Moreover, it shows the potential of controlling charge transport through electron-donating/-withdrawing side groups by using weak terminal binding or electronically decoupling the strong terminal binding.

Chapter 6

Molecular junctions based on aromatic coupling

If individual molecules are to be used as building blocks for electronic devices, it will be essential to understand charge transport at the level of single molecules. Most existing experiments rely on the synthesis of functional rod-like molecules with chemical linker groups at both ends to provide covalent or donor/acceptor anchoring to the source and drain contacts. This approach has proved very successful, providing quantitative measures of single-molecule conductance, and demonstrating rectification and switching at the single-molecule level. However, the role of intermolecular interactions has been overlooked. Here we compare break junction measurements of OPE molecules with terminal anchor group on both ends and the situations when there is only one single anchor group (OPE-monothiol molecules). We will discuss the influence of aromatic π - π coupling between adjacent molecules on the formation and operation of molecular junctions.

6.1 How about taking one anchor group away?

As we have seen in Chapter 5, a single molecule (or a few molecules) with two terminal anchor groups can be successfully linked in the gap between two atomic-scale gold contacts to form a molecular junction (Fig. 6.1a). Thiols (-SH) have been widely used as terminal anchor groups. Because the covalent Au-S bond is stronger than a Au-Au bond [48; 66], the Au atoms migrate to the ends of the contacts to form elongated tips when the electrodes are pulled apart (red arrows in Fig. 6.1b). This process continues until the force exceeds the strength of the Au-Au bond and the molecular junction breaks open. The electrical conductance of the junction remains approximately

constant as the electrodes are pulled apart during stretching and then drops suddenly when the molecular junction breaks open. The plateau features in conductance traces $G(z)$ below G_0 and the corresponding peaks in $\log G$ -histogram are expected as indications of signal of molecular junctions.

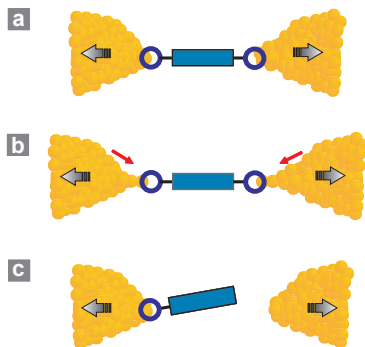


Figure 6.1: Anchoring of a molecule in a metal junction: (a) A stable molecular junction is realized when a molecule anchors between the Au metal electrodes with the aid of two chemical linker groups (emphasized with a circle) that form chemical bonds to the Au; (b) When the electrodes are moved apart, the Au atoms are pulled by the anchored molecule into the periphery of the Au junctions (arrows), leading to the formation of tips; (c) Molecules with only one anchor group are not expected to form a stable molecular bridge.

For molecules with only one anchor group rather than two, one would not expect a stable metal-molecule-metal junction because the molecules could only attach to one side of the junction (Fig. 6.1c). However, this assumption ignores intermolecular interactions and, as we shall see, these interactions can be relevant to the behavior of molecular junctions.

6.2 Molecular signal of OPEmonothiol molecules

We use oligo-phenylene ethynylene (OPE) molecules as our model system. Conjugated molecules such as OPE have interesting electron transport properties due to the delocalization of electrons along the molecular backbone [67; 68]. Such a structure results in the energy gap between the lowest unoccupied molecular orbital (LUMO) and the highest occupied molecular orbital (HOMO) being smaller (~ 3 eV) than the HOMO-LUMO gap of saturated

molecules (~ 7 eV), leading to a more efficient charge transport through the molecule.


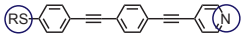
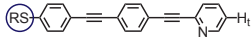
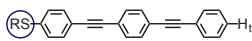
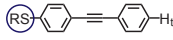
	Molecule	Length L (Å)	No. of samples	Conductance $G(G_0)$
1		20.7 (S-S)	4	$(1.2 \pm 0.1) \cdot 10^{-4}$
2		18.7 (S-N) 19.4 (S, Lp)	3	$(5.7 \pm 2.4) \cdot 10^{-5}$
3		19.8 (S- H_t)	3	$(6.6 \pm 1.3) \cdot 10^{-6}$
4		19.8 (S- H_t)	3	$(5.9 \pm 2.4) \cdot 10^{-6}$
5		12.9 (S- H_t)	4	-

Table 6.1: Molecules investigated and related parameters. The molecular rods **1-5** were synthesized in their acetyl-protected form ($R=\text{COCH}_3$). *In situ* deprotection formed the free thiol which coordinated to the Au electrodes ($R=\text{Au}$). The different anchoring groups are highlighted (\bigcirc). *Lp* refers to the nitrogen lone pair and H_t denotes the terminal hydrogen. The length of each molecule is obtained after energy minimization using the MM2 force field (ChemDraw 3D). The single molecule conductance value G is deduced from the peak that appears in the $\log G$ -histograms of 100 opening $G(z)$ -curves obtained from 3-4 different samples.

The molecules (**1-5**) displayed in Table 6.1 were designed and synthesized for the charge transport characterization reported here. The table illustrates as well the strategy of the present study. Using three-phenyl-ring OPE molecules, we gradually change the strength of the molecular linker on one end of the molecule. Molecule **1** is our reference OPE-dithiol molecule, which has two terminal thiol anchors to covalently bridge the two contact electrodes. This molecule does form single molecule junctions [58]. In molecule **2**, a pyridine-nitrogen atom on the *para* position of the terminal phenyl ring replaces the thiol anchor group. Here, one may still expect the formation of single molecule junctions, due to the coordination of the nitrogen atom with the Au electrode [64; 66; 69]. In molecule **3**, the nitrogen atom is “hidden”, by shifting it from *para* to *ortho* position within the phenyl ring, which should drastically reduce the binding properties of the molecule. Finally, the second anchor group is completely removed in **4**. Molecule **5** is a shorter derivative and serves as an additional control to complete the series. The result of the corresponding conductance measurements are shown

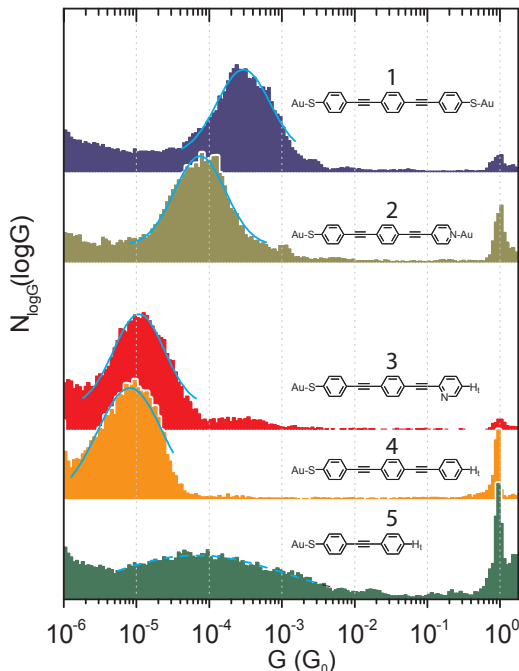


Figure 6.2: Conductance histograms for the different molecules. Comparison of $\log G$ -histograms for OPE molecules with two linking terminals (molecules **1** and **2**), and with only one thiol linker (molecules **3** through **5**). Each histogram was built from 100 conductance traces obtained during successive opening cycles. The pronounced Gaussian-like peaks (solid lines) in the $\log G$ histograms represent the signatures of the specific molecule investigated. The molecular junction conductance is deduced from the peak conductance G_{peak} .

in Fig. 6.2 (linear histograms are shown in Appendix B.2). The order of molecules is alike to that in Table 6.1. It is immediately evident, that in all cases a pronounced conductance peak appears. It is surprising that both the height and the width of these peaks are similar for molecules **1-4**. Going through the sequence from above, we see that the conductance value G_{peak} , corresponding to the peak position in the $\log G$ histogram, is for molecule **2** slightly reduced by approximately a factor of 2-3 as compared to molecule **1**. This lower value is due to weaker electronic coupling between nitrogen and Au atoms as discussed in Section 5.1.

Whereas we expect a peak in $\log G$ histogram for molecule **2**, a similar peak of equal magnitude for molecule **3** comes as a surprise. Because the nitrogen atom of the pyridine structure is in molecule **3** “hidden”, it may provide, if at all, a much less probable binding site to the electrode. Contrary to this, the identical magnitude and width of the peak in $\log G$ histograms suggest that also molecule **3** binds in the junction with a similar probability as molecules **1** and **2**. Hence, the observed strong binding must have another origin. This is supported further by the measurements for molecule **4**. Although the anchor group at one end is now removed, we obtain very similar results for **3** and **4**. Why does a molecular junction form, even with molecular rods having only a single linker group on one side of the rod?

6.3 The interpretation: π - π stacking

We think that the connection between the electrodes is made possible by π - π stacking interaction between a pair of molecules [70; 71; 72]. If one molecule is anchored via its thiol linker group on e.g. the left electrode, another one bound to the right electrode can complete the mechanical assembly of the junction via π - π coupling through the phenyl rings. This interpretation is supported by the shift of G_{peak} to lower values by more than an order of magnitude. In this picture, a reduced G value is expected because the pair of molecules will be longer than a single dithiol molecule anchored between Au electrodes. We observe that the junctions form with a similar probability, whether for dithiolated compounds or monothiolated compounds. This might *a priori* appear surprising since the molecular junctions formed by monothiolated compounds will be composed by two molecules and might therefore occur less frequently. This is however not the case since we do not have a diffusion-limited experimental situation. After immersion in the molecular solution, the Au bridge will be covered with a monolayer of molecules on its whole surface. Upon breaking the Au bridge open, there will be a high local concentration of molecules available for the formation of a molecular junction. While the kinetics of junction formation will depend on whether we have dithiolated or monothiolated compounds, the typical time constants will be orders of magnitude faster than what our experimental setup can resolve (typically 5 ms). We therefore do not expect to see a difference between both situations.

Since the strength of π - π stacking depends strongly on the conjugation extent of the system and the overlap between adjacent compounds, one straightforward control experiment, without modifying largely the electronic structure of the molecules, is to investigate an OPE compound with only

2 phenylene units (molecule **5**). Here, the width of the conductance peak in the $\log G$ histogram is much broader than any other molecule has shown before, see Fig. 6.2. While this peak is also somewhat shallow, single $G(z)$ -curves still display clearly visible but noisier plateaus at values larger than the plateau values for molecules **3** and **4** (see Appendix B.2). We think that the peak for molecule **5** is less pronounced because of the reduced π - π interaction for these shorter molecules, leading to a mechanically less stable junction. Note that a pair of molecules **5** tends to have a higher conductance value than a pair of molecules **4** because of the reduced distance the electrons have to tunnel between the Au electrodes through the molecular bridge. We also emphasize that without deprotecting the thiol function, no molecular signature can be detected in the break junction. This permits to eliminate other unanticipated interactions but intermolecular interactions to explain the signal observed for compounds **3-5**. Finally, we also checked that for compounds where no aromatic stacking is possible, such as monothiolated alkane chains, we do not observe the formation of molecular junctions (see Appendix B.2). These experiments clearly reveal the importance of the immediate surrounding in transport molecular junctions involving single or a few molecules [73; 74; 75; 76].

6.4 Tunneling picture

As briefly stated above, the different conductance values can qualitatively be attributed to the difference in the distance that electrons have to tunnel between the Au electrodes. This distance is determined by the length of a single molecule if there are anchors on both sides, or by the length of π - π stacked pair of molecules otherwise. The stacking of a pair of monothiol molecules **3** is illustrated in Fig. 6.3a. Fig. 6.3b-d sketches different stacking configurations of the same molecule, whereas Fig. 6.3e shows the two-side anchored dithiol molecule.

By considering the σ -framework and the π -electrons separately, Hunter and Sanders [77] emphasized that the geometrical arrangement of interacting aromatic molecules is essentially governed by electrostatics. Two aromatic molecules brought in close proximity will not register directly on top of each another due to the electrostatic repulsion of the negative π electron clouds. A net positive interaction will result from the π - σ attraction, translating for instance in a staggered face-to-face configuration as shown in Fig. 6.3a. The question of the relative orientation of the aromatic rings within an OPE molecule remains a matter of debate. The fully planar configuration has the minimum energy [73; 78; 79]. In diluted solution at room temperature,

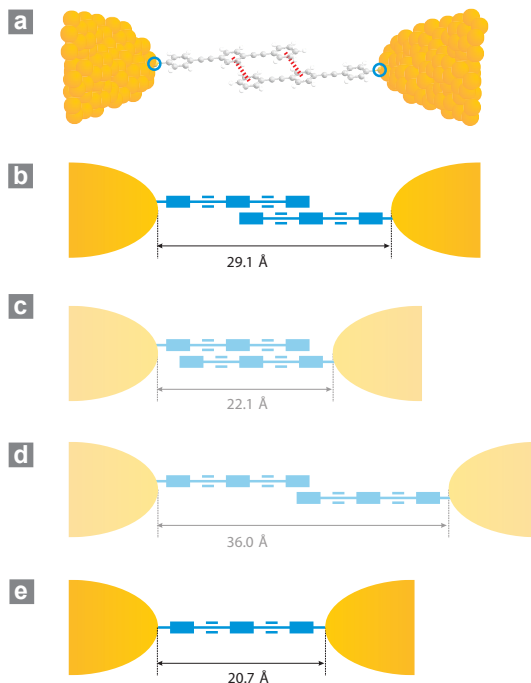


Figure 6.3: Illustration of possible stacking configurations: (a) Staggered π - π stacking configuration of a pair of OPE-monothiol molecules within which the aromatic rings are shifted by half of the ring length; (b)-(e) Simplified representation of different configurations of OPE molecules between the electrodes. A rectangle indicates a phenyl ring: (b) The configuration anticipated as the most probable one; (c,d) Less probable configurations due to steric hindrance (c) and reduced conjugation and overlap (d); (e) A single OPE-dithiol molecule between electrodes. All distances are taken between the sulfur atoms on both sides and were estimated after minimizing the energy of the compound via a molecular mechanics calculation using the MM2 force field (ChemDraw 3D).

experiments and calculations suggest however that the aromatic rings of OPE molecules are able to explore different orientations [78; 80]. This is certainly true at low concentration. At higher concentrations, where the π - π interaction induces aggregation, coplanar stacking appears favored [79; 81; 82]. This is also the case in crystals of similar aromatic compounds [83; 84]. In our case, the molecules self-assemble at the surface of the Au electrodes,

leading to a high local concentration. We therefore expect the molecules to form coplanar stacks as illustrated in Fig. 6.3a. Fig. 6.3b-d depict possible stacking configurations. We think that Fig. 6.3a,b represents the actual stacking configuration of a pair of molecules **4**. Structures 4c and 4d are seen as less probable because of steric hindrance and because of the weaker π - π interaction due to the reduced overlap between the molecules.

In a simple tunneling picture where electrons tunnel through an effective medium over a distance d , the conductance G can be written as $G = A \cdot e^{-\beta d}$. The decay constant β is determined by the electronic parameters of the effective medium (here, the molecules). For a given electrode material (here, Au), the pre-factor A depends on the electron density-of-states at the point where the molecule contacts the Au electrode. Because this is determined by thiol anchors both in single molecule and stacked pair of molecules, this factor can be taken as a constant. Note that in this tunneling picture, the symmetric and constant peak widths in the $\log G$ histograms (Fig. 6.2) reflect the fact that the conductance fluctuations mainly arise due to variations in the exponent of the conductance. The conductance fluctuations can therefore be attributed to variations of the effective tunneling distance d and the decay constant β as generated by local changes in the geometrical arrangement of the molecular junction. Experimental and theoretical evidence have already been provided for a strong through-space conjugation between π systems that were held together via carbon linkers [85]. For the following estimate we will use a typical average decay constant of 0.3 \AA^{-1} for the OPE derivatives as obtained from electron transfer rates in donor-bridge-acceptor systems [86; 87; 88] and theory [89; 90]. The distances between the two sulfur atoms are 20.7 \AA for the single OPE-dithiol molecule (Fig. 6.3e) and 29.1 \AA for a pair of OPE-monothiols (Fig. 6.3b). The longer tunneling distance between electrodes for a stacking junction leads to a 12 times lower conductance. This is in reasonable agreement with the experiment which shows a 20-fold difference.

6.5 Conclusion

In conclusion, we have demonstrated that intermolecular π - π stacking interaction between monothiol molecules composed of alternating phenylene and ethynylene units is strong enough to induce the formation of molecular junctions. The yield is similar to that of dithiol molecules with a molecular signature reaching the same degree of quality as judged from the statistical variation of single junction conductance values. This is a significant finding for molecular electronics. Intermolecular aromatic stacking plays a

determinant role in stabilizing nano-objects. The importance of π - π overlap has long been recognized in thin-film organic electronics, molecular mechanics, and especially in biomolecular and supramolecular chemistry. We show here that π - π stacking can also be used as the dominant guiding force for the formation of molecular bridges in few molecules electronic junctions. These experimental findings provide a strong ground for the design of future electro-mechanical and sensing devices operating at the single molecule level.

Chapter 7

Controlling charge transport through redox molecules

The understanding and control of charge transport properties of molecular electronic junctions and devices is an ultimate goal of molecular electronics. Simple conjugated molecules such as OPEs may function as passive molecular wires as we have already seen in previous chapters. We further consider how to implement electronic functions in molecular junctions such as switches, transistors, rectifiers, etc.. A broad range of design strategies have been used or proposed, for example, for molecular rectifiers by taking use of asymmetric electron-donor/electron-acceptor (or electron-rich/electron-poor) subunits [34; 91; 92; 93]; Light-triggered switches based on change of conjugation [41; 94; 95; 96]; Electrochemical active switches with controlled redox states [28; 29; 97; 98; 99] (see also review papers [100; 101; 102; 103]); And potential sensing devices by reaction of integrated molecules with an analyte [104; 105; 106].

In this chapter we will study charge transport of redox molecules in our break junctions. Different oxidation states of a redox molecule can be obtained either by the use of oxidizing agents or electrochemistry. In the first section we describe the conductance measurement of a tetrathiafulvalene (TTF) derivative in its neutral and radical states by simple chemical oxidation. In the second section, an electrochemical gate is applied *in situ* to tune conductance of a ferrocene (Fc) derivative.

7.1 A tetrathiafulvalene derivative under chemical oxidation

Tetrathiafulvalene (TTF) and its derivatives are famous as π -electron donors for electron transfer system [107; 108]. In its neutral state, TTF is a non-aromatic 14- π -electron system; it readily loses electrons sequentially in the presence of oxidizing agent (for example an Fe^{3+} compound) to form a radical cation ($\text{TTF}^{+\bullet}$) and a dication specie (TTF^{2+}). The process is reversible by adding reducing agent (for example a ferrocene compound). In electrochemistry, cyclic voltammogram (CV) of a TTF shows two reversible peaks as indication of the three-state redox process. After oxidation, both of the charged states are stable due to the formation of 6 π - and $2 \times 6\pi$ - electron heteroaromaticity of the 1,3-dithiolium cation (illustrated in Fig. 7.1a).

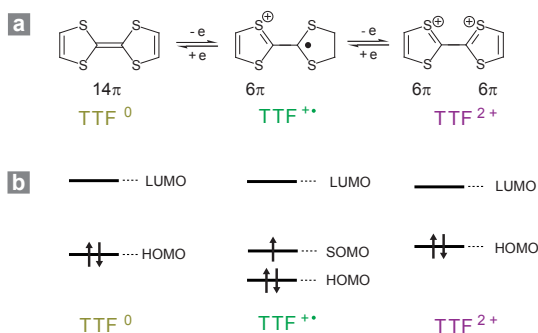


Figure 7.1: (a) A TTF molecule in its neutral (TTF^0) and oxidized states (radical cation $\text{TTF}^{+\bullet}$ and dication TTF^{2+}). Both of the charged states are stable due to the formation of 6 π - and $2 \times 6\pi$ - electron heteroaromaticity of the 1,3-dithiolium cation; (b) Schematics of corresponding molecular orbitals. A SOMO (Single Occupied Molecular Orbital) state appears at its radical cation state.

There are therefore three reversible states from the same molecule: neutral, radical cation and dication. Different charged states usually have different electronic structures such as different HOMO-LUMO gaps, and a single occupied molecular orbital (SOMO) state appearing at radical cation state (Fig. 7.1b), which make their transport properties interesting.

7.1.1 Characterization of chemical oxidation

Fig. 7.2a shows the structure of the molecule studied in this work: alkane thiol chains (with 3 carbon atoms) are attached to TTF core through a sulfur

atom. There are two isomers with 1:1 ratio according to different binding positions. The reversibility of the redox states can be characterized by CV and photoelectrochemistry (see Appendix B.3).

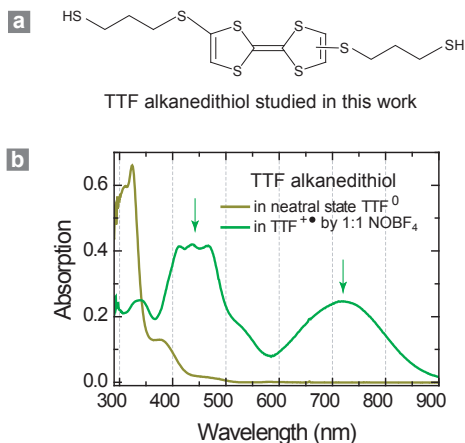


Figure 7.2: (a) Structure of TTF derivative studied in this work. Alkane thiol chains (with 3 carbon atoms) are attached to TTF core through a sulfur atom. There are two isomers with 1:1 ratio according to different binding positions (sulfur atom on the right side binds either on up or down carbon atom); (b) UV-vis spectrum of the neutral TTF derivative in dichloromethane (DCM) and the same solution after adding in 1:1 oxidizing agent NOBF₄. Neutral TTF derivative absorbs around 320 nm, while two new absorption bands appear (peaks at 450 nm and 720 nm indicated by arrows) for the radical cation state TTF^{•+}.

It is known that an Fe³⁺Cl₃⁻ compound is an ideal oxidizing agent for TTF core structure [109], but we can not use it to oxidize our TTF alkanedithiol here because it coordinates immediately with free thiols and precipitates as green powders. This effect limits our choices of oxidizing agents to be non-metals. Finally we find out that nitrosonium tetrafluoroborate (NOBF₄) can oxidize the TTF derivative to the TTF^{•+} state, and at the same time, does not react with the free thiols. The reaction can be characterized clearly in UV-vis spectrum (Fig. 7.2b). Neutral TTF derivative absorbs around 320 nm, while two new absorption bands appear at 450 nm and 720 nm for the radical cation state TTF^{•+} [110; 109]. In the meantime, the color of the solution turns from yellow to green.

However, the oxidized state turns out to be unstable in air. The two-band absorption of the TTF^{•+} decays gradually upon time and even more

dramatically with adding in more NOBF_4 . This may due to the change of chemical environment after decomposition of NOBF_4 . The NOBF_4 is very sensitive to water or even moist air and can decomposes to nitrous acid (HNO_2), which may then lead to the decomposition of TTF structure. It is therefore important to use dry solvent and keep the atmosphere under Ar.

7.1.2 Molecular conductances of the neutral and radical cation states

We first try to immobilize the TTF-alkanedithiol in break junctions. Typical conductance traces $G(z)$ and $\log G$ histogram of 0.06 mM neutral TTF derivative in dichloromethane are shown in Fig. 7.3a and b. Molecular plateaus tend to appear between $1 \cdot 10^{-4}$ and $1 \cdot 10^{-5} G_0$ but with low yield ($\leq 20\%$). The histogram built from 100 consecutive opening curves therefore does not show a clear Gaussian peak, but rather in a shape of slope. The molecular signal of the TTF derivative is not as well defined as compared with typical OPE families that we have seen in previous chapters or octanedithiol that we have measured before (both with plateaus yield of 40 – 50 %). More tests with higher concentration (0.6 mM) in mesitylene solvent have also been carried out and the results (see Appendix B.3) are quite similar as in the case of DCM.

Nevertheless we tested the radical cation state of the TTF alkanedithiol in break junctions by using chemical oxidation. A concentrated TTF alkanedithiol/DCM solution is degassed with bubbling of Ar for 10 min, then a 1:1 ratio of NOBF_4 is added. A certain amount of the solution of oxidized molecules which corresponds to the final 0.06 mM concentration is carefully transferred into the liquid cell which contains pure degassed DCM and there is constant Ar bubbling during the measurement.

The typical conductance traces and $\log G$ histogram of $\text{TTF}^{+\bullet}$ are shown in Fig. 7.3c and d, where molecular signals are better visible. We observed that in some cases there is a strong tunneling decay background in single $\log G(z)$ curves (guided by gray dash lines). This feature leads to the large constant background in histogram (guided by gray dash lines) and a small peak showing up at $1 \cdot 10^{-4} G_0$ as the indication of molecular signal.

7.1.3 Discussion

Based on our measurements, the neutral TTF alkanedithiol does not exhibit clear molecular signal (i.e. peaks in $\log G$ histogram). There can be several reasons: first of all, it is possible that the thiol-linking signal is below our measurement resolution (the resolution can reach $1 \cdot 10^{-6} G_0$ in mesitylene as shown in Appendix B.3). Secondly, there can be other binding possibilities

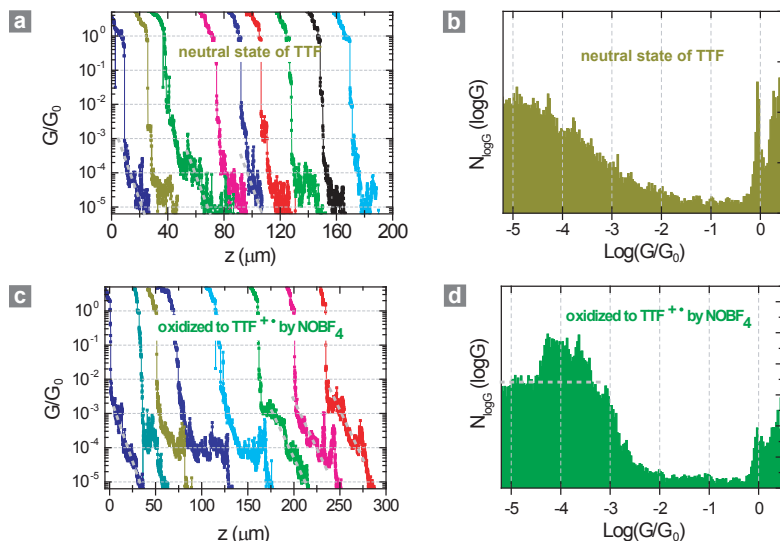


Figure 7.3: (a) and (b) are typical conductance traces $G(z)$ and $\log(G)$ histogram of 0.06 mM/DCM neutral TTF alkanedithiol. The plateaus are not well defined and the values disperse, leading to a slope-shape in histogram; (c) and (d) are typical conductance traces $G(z)$ and $\log(G)$ histogram of 0.06 mM TTF/DCM derivative in the state of TTF $^{+\bullet}$; A small peak at $1 \cdot 10^{-4} G_0$ shows molecular signal and dash lines indicate the tunneling background.

apart from thiols. The molecule contains 6 sulfur atoms apart from the thiol linkers and 14- π electrons in the core of TTF. They can also have interactions with gold electrodes. For example, as shown in a recent publication that methyl sulfides can also link properly with gold electrodes [61]. These effects contribute more but poorly defined binding possibilities, and their roles in the transport property are not known.

In the situation of radical cation, there is only one sigma bond at the center of TTF. The two rings can therefore rotate relative to each other which weakens the interaction between TTF core and gold electrode, leading to better defined thiol-linking properties. The strong tunneling background as we observe in Fig. 7.3c and d may come from different conformations of alkane structures (for example, adaption from gauche- to trans-) which leads to variable tunneling distance.

7.1.4 Concluding comments

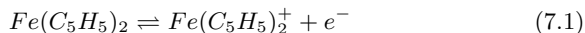
In summary we have carried out a preliminary transport study of a TTF-alkanedithiol derivative in its neutral and radical cation states by the method of chemical oxidation. There is a hint that the junction shows conductance of $1 \cdot 10^{-4} G_0$ in its radical cation state. But quantitative comparison with its neutral state is not possible since there is no well defined molecular signal in its neutral state.

Chemical oxidation/reduction is an easy way to reach different redox states of molecules. Relating this property to charge transport of molecular junction provides potential application for chemical sensing and molecular switching. Its disadvantages in break junction measurement are limitation of compatible oxidation agents and lack of convenient reversible control.

7.2 Conductance of a ferrocene derivative tuned by electrochemical gate

An organometallic moiety has a complicated 3D structure which is very different from a simple carbon-hydrogen chain compound. In a ferrocene (Fc) molecule, an iron atom is sandwiched between two cyclopentadienyl (Cp) rings (cf. the central core of OPVFc in Fig. 7.4a). The iron atom is in the 2+ oxidation state (Fe^{2+}), while each 5-carbon Cp ring is one electron charged and therefore allocated 6 π -electrons and becomes aromatic. Combining the twelve electrons of the Cp rings (six from each) and the six d-electrons on Fe^{2+} results in an 18-electron, noble gas electron configuration. This makes the total ferrocene structure neutral and stable though the iron atom is charged.

Ferrocene is one of the most well studied redox molecules. The Fc/Fc^+ reaction is extensively used as calibration standard of potential in electrochemical measurements. By losing one electron, a Fc molecule can turn to its oxidation state Fc^+ at a low potential, around 0.5 V vs. a saturated calomel electrode (SCE) and the process is fully reversible:



These properties make Fc molecule an interesting model system for studying electron transport phenomena. How does an organometallic compound affect electron transport? More efficiently than simple conjugation based on carbon and hydrogen? Furthermore, can we tune the transport property by changing the redox state? In this section we first try to immobilize the ferrocene derivative in break junctions. Then we discuss the first results of electrochemical-gate controlled charge transport study.

7.2.1 What is the effect of an organometallic block?

Based on our knowledge of conjugated molecules, in this work, a ferrocene moiety is built into an OPV-type (oligo-phenylene vinylene) conjugated structure by substituting the central phenyl ring as illustrated in Fig. 7.4a (OPVFc). The structure of a normal OPV is also shown as comparison.

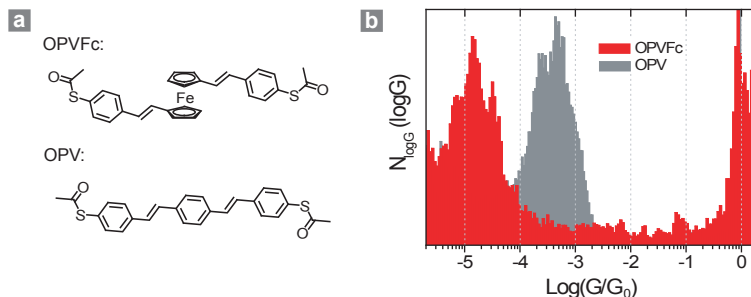


Figure 7.4: (a) Structure of a ferrocene derivative OPVFc and an standard OPV molecule with thiol anchor groups; (b) Comparison of $\log G$ histograms of OPVFc and OPV molecular junctions. Clear molecular signal is observed in both cases. The conductance value of an OPVFc junction is more than an order of magnitude lower than that of an OPV junction.

Conductance histograms of OPVFc and OPV after *in situ* deprotection are shown in Fig. 7.4b. It exhibits clearly that the conductance value of an OPVFc junction is more than an order of magnitude lower than that of a simple conjugated OPV junction. Quantitatively, the average conductance value of three distinct samples is $G_{OPVFc} = (7.6 \pm 2.7) \cdot 10^{-6} G_0$, which is ~ 25 times lower than that of an OPV junction ($G_{OPV} = (2.0 \pm 0.2) \cdot 10^{-4} G_0$).

After successful immobilization of OPVFc in break junctions, we will next try to control its conductance by applying an electrochemical gate.

7.2.2 An introduction to electrochemical gate

An universal way to control oxidizing/reducing states of redox molecules is through electrochemistry. There are only electrodes and electrolyte involved, making the system clean, and in addition, a reversible control is possible.

In classic electrochemistry, the potential of an electrode can be biased with respect to a reference electrode potential to reach the HOMO/LUMO states of redox molecules to oxidize/reduce the molecules [5]. This approach has been adapted to control electron transport through a single redox molecule

by placing the molecule in between source/drain electrodes [28; 29; 97; 98; 99].

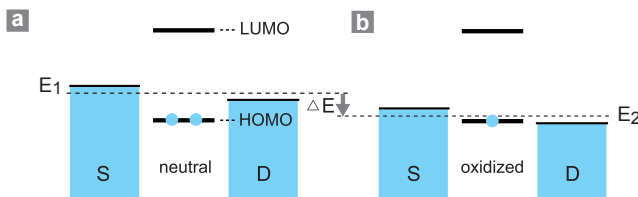


Figure 7.5: Schematics of the principle of an electrochemical gate¹: The chemical potential of source-and-drain electrodes can be tuned referred to a reference electrode from E_1 in (a) to E_2 in (b). When the potential of source-and-drain electrodes reaches HOMO level of the molecule, the molecule is then oxidized by losing one electron to electrodes (here the drain electrode), showing high barrier transparency in this case. The oxidizing/reducing process is reversible by sweeping ΔE in opposite directions.

The molecular junction is immersed in an electrolyte, then the potential of source-and-drain electrodes can be adjusted relative to the potential of a reference electrode, for example in Fig. 7.5 by ΔE , to be close to molecular HOMO level and oxidize the molecule by getting one electron from it. At the same time, a small bias voltage (max. 100 mV) is applied between source/drain electrodes to access electron transport properties through the molecule. We can expect that now at the molecular oxidation state, the device should show a high barrier transparency and display promising functional behaviors such as switches. The process is easily controlled reversibly by sweeping ΔE in opposite direction to reduce the radical molecule back to its neutral state. In this case, the potential drop between reference electrode and source-and-drain electrodes is called gate voltage and the reference electrode is therefore called a “gate electrode” (for technical details see Section 3.3).

¹In the language of electrochemistry as the author uses here, the potential of the reference electrode is considered to be zero. The gate voltage is applied to shift the chemical potential of source-and-drain electrodes by polarizing the electrode/electrolyte interface (c.f. Section 3.3); In the language of quantum dot gating, as the source electrode is grounded, it considered to be zero potential. The role of the gate voltage applied between reference electrode and source-and-drain electrodes is to tune the HOMO/LUMO levels of redox molecules. The illustration of electrochemical gate in the latter case would be the other way around in Fig. 7.5. In the sense of tuning molecular orbitals relative to the potential of source-and-drain electrodes, we think both descriptions are correct.

7.2.3 Molecular conductance controlled by the electrochemical gate

A quasi-reference electrode (Pt/Ppy) is fabricated by a Pt wire coated with partially oxidized polypyrrole (Ppy) in our experiment since standard reference electrodes such as Ag/AgCl and SCE are not suitable for working in organic solvents. The Pt/Ppy reference electrode is easily fabricated by cyclic voltammetry (CV) with the metal electrode in an acetonitrile or DCM solution of 10 mM pyrrole containing 0.1 M Bu₄NPF₆ electrolyte (tetrabutylammonium hexafluoro-phosphate). This Pt/Ppy quasi-reference electrode is much more stable than the widely used metal (e.g., Ag, Pt) wire and can work in both aqueous and organic media [111]. Further details of the fabrication are described in Appendix C.3.

The gate voltage between source-and-drain and reference electrodes is applied through a custom made potentiostat which responds rapidly to changes of local environment and keep the difference as set. In our case, positive gate potential moves the E_F down to HOMO level of Fc and the molecule therefore reaches its oxidation state. Correspondingly, the oxidized OPVFc⁺ can be reversed to its neutral state (OPVFc) by applying negative gate potential.

Conductance histograms of OPVFc molecular junctions show changes at different gate potentials (Fig. 7.6a). There is a tendency that at positive potentials, the main peaks of an oxidized OPVFc junction appear at higher conductance values; and at negative potentials, a neutral OPVFc junction has low values. The conductance values of two samples under different gate potentials are summarized in Fig. 7.6b. Also plotted is the case when no gate potential is applied, in which the conductance value is close to that of a gate-controlled neutral OPVFc junction. The increase of approximately eight times in conductance value is found for the oxidized OPVFc relative to its neutral state.

An *in situ* CV curve provides the evidence for the redox state of the molecules at different gate potentials. When the OPVFc is in neutral state, there is principally no charge transfer to the source or drain electrode and the current should be nearly zero (practically small current is observed due to the impurities such as remained water and oxygen). In contrast, a striking increase of current takes place when the gate potential becomes enough to oxidize the OPVFc and many OPVFc molecules start to give electrons to source-and-drain electrodes (to limit this current we use polyimide-covered break junction as described in Section 3.3.3. Fig. 7.6b (with the right axis) shows the oxidation process occurs at 0.2 V vs. Pt/Ppy quasi-reference electrode. Combining the changes of conductance values, it reveals that the increase of conductance is indeed attributed to the oxidation of the Fc moiety.

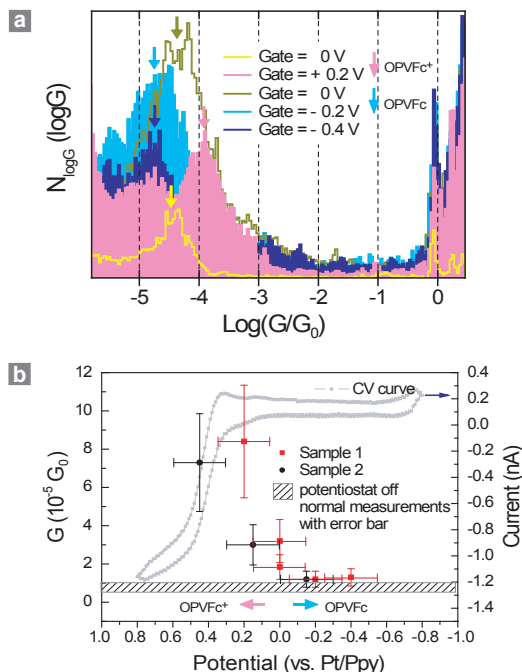


Figure 7.6: (a) Comparison of conductance histograms of OPVFc molecular junctions at different gate potentials. Positive potentials are first applied to oxidize OPVFc and the main peaks of molecular signal tend to shift to high conductance values; Then the gate potential is set back to zero and then to negative direction to reduce iron atom to be neutral OPVFc. At the same time, the conductance peaks tend move to lower values. The conductance values shown in (b) are taken from the Gaussian fit of main peak of $\log G$ -histograms and transformed back to linear scale. There are in some cases two peaks in histogram, for example with Gate = 0.2 V, the conductance value is taken from the main peak (as indicated by arrows); (b) Comparison of conductance values of OPVFc molecular junctions in two samples under gate potentials and in the case when there is no gate potential applied. The error bars of conductance values are derived from the standard deviation of three measurements without gate potential. The error bars of gate potentials are estimated from the redox potential difference of OPVFc in two samples by using two distinct Pt/Ppy reference electrodes ($= \pm 0.15$ V). An *in situ* cyclic voltammogram shows the increasing of conductance indeed corresponds to the oxidation of the Fe Cc unit.

7.2.4 Discussion

The immobilization measurements show that although the two Cp rings can have certain freedom of rotation relative to each other, the molecular signal of an OPVFc junction is as well defined as compared with a rigid OPV junction. Our data suggests that the OPVFc tends to have linear configuration and eventually binds with the electrodes with the two terminal thiol anchor groups.

We have also observed that the conductance value of an OPVFc junction is more than an order of magnitude lower than that of a simple conjugated OPV junction, indicating that the 3D ferrocene building block bring an extra through-space tunneling barrier. This experimental finding is however in conflict with the measurement based on a fabricated gold nanogap junction, where a near-perfect metallic conduction was observed [112]. We think that in a fixed-gap molecular junction, the error may be induced by the failure of contacts.

Moreover, by applying an electrochemical gate potential to the molecular junction, the chemical potential of source-and-drain electrodes slowly approaches to the HOMO level of ferrocene until the molecule loses one electron to the electrode to be oxidized, or HOMO/LUMO levels shift until the HOMO level reaches the energy of source-and-drain electrodes. Correspondingly, the molecular conductance tends to increase until it shows a jump when the ferrocene moiety reaches its oxidized state. Qualitatively, the experimental observation can be explained by a resonant single occupied tunneling level generated by the oxidation of ferrocene moiety.

7.2.5 Concluding comments

In conclusion we have successfully immobilized a ferrocene-OPV-dithiol compound in break junctions. We have found out that electron transport in a ferrocene embedded conjugation structure is less efficient than a simple 2D conjugated backbone structure.

We have preliminarily demonstrated in our break junction setup that an electrochemical gate can be applied to control the charge transport in single redox-active molecules. For the OPV-ferrocene-dithiol junction, approximately eight times higher conductance value is observed for the oxidized state and the process is reversible and repeatable, which can form the basis for single molecule switches or transistors.

Chapter 8

Conclusion and outlook

In this thesis we were able to successfully immobilize various conjugated oligomers in our break junctions. Signals of different molecular junctions can be compared via a robust statistical analysis based on conductance histograms. By using conjugated oligo-phenylene ethynylene (OPE) or oligo-phenylenevinylenes (OPV) as our model system, we have systematically studied the role of contacts and the effects of substituted groups in molecular conductance. Very interestingly, by using OPE molecules with only one anchor group, we have discovered a new type of molecular junction which is based on intermolecular π - π interaction. Furthermore, we have demonstrated that it is possible to control the conductance of a redox molecular junction by an electrochemical gate.

Our experimental findings suggest that a deeper insight into the band alignment of molecular orbitals is crucial for the understanding of conductance values of molecular junctions. Combination of spectroscopy such as I - V measurements during the stretching of molecular junctions would be much preferential. The challenge of I - V measurements at room temperature and in liquid environment is to avoid the disturbance of electrochemical reactions of impurities such as water and oxygen. To minimize the disturbance, we need to further reduce the junction area which is exposed in liquid or use small liquid cell which allows better control of inert environment.

New concepts are required for future development of single-molecule electronics. Based on the understanding of anchoring properties and band alignment of molecular orbitals, gating effects can be applied by inserting electron donor/acceptor substitutes to the molecular backbone structure. Different electronic functions mimicking switches, diodes and memory elements can be accessed via alteration of molecular structures (e.g. conjugation or conformation). Strategies based on quantum phenomena such as phase interference

also provide potential realization of novel electronic functions [113].

Furthermore, in the view of possible application of single-molecule electronics, much effort needs to be put in the reliable fabrication and stabilization of molecular junctions in order to integrate them into electronic circuits.

Bibliography

- [1] G. E. Moore, Electronics **38**, 8 (1965).
- [2] A. Aviram and M. A. Ratner, Chem. Phys. Lett. **29**, 277 (1974).
- [3] M. A. Reed, C. Zhou, C. J. Muller, T. P. Burgin, and J. M. Tour, Science **278**, 252 (1997).
- [4] B. Xu and N. J. Tao, science **301**, 1221 (2001).
- [5] A. J. Bard and L. R. Faulkner, *ELECTROCHEMICAL METHODS Fundamentals and Applications*, John Wiley and SONS, Inc., 2001.
- [6] N. Agraït, A. L. Yeyati, and J. M. van Ruitenbeek, Phys. Rep. **377**, 81 (2003).
- [7] R. Landauer, Phil. Mag. **21**, 863 (1970).
- [8] R. Landauer, Phys. Scr. **T42**, 110 (1992).
- [9] D. Wharam et al., J. Phys. C **21**, L209 (1988).
- [10] B. van Wees et al., Phys. Rev. Lett. **60**, 848 (1988).
- [11] H. Ohnishi, Y. Kondo, and K. Takayanagi, Nature **395**, 790 (1998).
- [12] Y. Imry, *Physics of mesoscopic systems*, World Scientific, Singapore, 1986.
- [13] R. de Picciotto, H. L. Stormer, L. N. Pfeiffer, K. W. Baldwin, and K. W. West, Nature **411**, 51 (2001).

- [14] C. Goldman, Phys. Rev. A **43**, 4500 (1991).
- [15] C.-P. Hsu and R. A. Marcus, J. Chem. Phys. **106**, 584 (1997).
- [16] S. Datta, *Electronic Transport in Mesoscopic Systems*, Cambridge University Press, 1st edition, 1995.
- [17] H. M. McConnell, J. Chem. Phys. **35**, 508 (1961).
- [18] A. Salomon et al., Adv. Mater. **15**, 1881 (2003).
- [19] B. Giese, M. Spichty, and S. Wessely, Pure Appl. Chem. **73**, 449 (2001).
- [20] S. H. Choi, B. Kim, and C. D. Frisbie, Science **320**, 1482 (2008).
- [21] F. Zahid, M. Paulsson, and S. Datta, *Electrical Conduction in Molecules*, Academic Press, 2003, Chapter published in "Advanced Semiconductors and Organic Nano-Techniques".
- [22] Y. Loo, R. Willett, K. Baldwin, and J. Rogers, J. Am. Chem. Soc. **124**, 7654 (2002).
- [23] T. Dadosh et al., Nature **436**, 677 (2005).
- [24] J. Liao, L. Bernard, M. Langer, C. Schönenberger, and M. Calame, Advanced Materials **18**, 2444 (2006).
- [25] B. Xu and N. J. Tao, Science **301**, 1221 (2003).
- [26] L. Grüter, M. González, R. Huber, M. Calame, and C. Schönenberger, Small **1**, 1067 (2005).
- [27] L. Grüter et al., Nanotechnology **16**, 2143 (2005).
- [28] X. Li et al., Faraday Discuss. **131**, 111 (2006).
- [29] Z. Li et al., Faraday Discuss. **131**, 121 (2006).
- [30] L. Venkataraman, J. E. Klare, C. Nuckolls, M. S. Hybertsen, and M. L. Steigerwald, Nature **442**, 904 (2006).
- [31] J. Reichert et al., Phys. Rev. Lett. **88**, 176804 (2002).
- [32] H. B. Weber et al., Chem. Phys. **281**, 113 (2002).
- [33] C. Kergueris et al., Phys. Rev. B **59**, 12505 (1999).

- [34] M. Elbing et al., PNAS **102**, 8815 (2005).
- [35] E. Lörtscher, J. W. Ciszek, J. Tour, and H. Riel, Small **2**, 973 (2006).
- [36] E. Lörtscher, H. B. Weber, and H. Riel, Phys. Rev. Lett. **98**, 176807 (2007) **98**, 176807 (2007).
- [37] R. Ochs, D. Secker, M. Elbing, M. Mayor, and H. B. Weber, Faraday Discuss. **131**, 281 (2006).
- [38] J. J. Park et al., Phys. Rev. Lett. **99**, 026601 (2007).
- [39] J. Reichert, H. B. Weber, M. Mayor, and H. v. Lili $\frac{1}{2}$ hneysen, Appl. Phys. Lett. **82**, 4137 (2003).
- [40] R. H. M. Smit et al., Nature **419**, 906 (2002).
- [41] D. Dulić et al., Phys. Rev. Lett. **91**, 207402 (2003).
- [42] J.-H. Tian et al., JACS **128**, 14748 (2006).
- [43] J. M. van Ruitenbeek et al., Rev. Sci. Instrum. **67**, 108 (1996).
- [44] S. A. G. Vrouwe et al., Phys. Rev. B **71**, 035313 (2005).
- [45] C. Untiedt et al., Phys. Rev. B **66**, 085418 (2002).
- [46] J. K. Gimzewski and R. Mili $\frac{1}{2}$ ller, Phys. Rev. B **36**, 1284 (1987).
- [47] M. Steinacher et al., The autoranging i to v converter, to be published.
- [48] Z. Huang, F. Chen, P. Bennett, and N. Tao, J. Am. Chem. Soc. **129**, 13225 (2007).
- [49] B. Xu, X. Xiao, and N. Tao, J. Am. Chem. Soc. **125**, 16164 (2003).
- [50] J. M. Krans et al., Phys. Rev. B **48**, 14721 (1993).
- [51] J. M. Krans, J. M. van Ruitenbeek, V. V. Fisun, I. K. Yanson, and L. J. de Jongh, Nature **375**, 767 (1995).
- [52] X. D. Cui et al., Science **294**, 571 (2001).
- [53] W. Haiss et al., pccp **6**, 4330 (2004).
- [54] X. Li et al., J. Am. Chem. Soc. **128**, 2135 (2006).
- [55] X. Xiao, B. Xu, and N. J. Tao, Nano Letters **4**, 267 (2004).

- [56] X. Xiao, L. A. N. amd A. M. Rawlett, and N. J. Tao, *J. Am. Chem. Soc.* **127**, 9235 (2005).
- [57] Z. Li et al., *Nanotechnology* **18**, 044018 (2007).
- [58] R. Huber et al., *J. Am. Chem. Soc.* **130**, 1080 (2008).
- [59] M. T. González et al., *Nano Letters* **6**, 2238 (2006).
- [60] F. Chen, X. Li, J. Hihath, Z. Huang, and N. J. Tao, *J. Am. Chem. Soc.* **128**, 15874 (2006).
- [61] Y. S. Park et al., *J. Am. Chem. Soc.* **129**, 15768 (2007).
- [62] L. Venkataraman et al., *Nano Letters* **7**, 502 (2007).
- [63] S. McDermott, C. B. George, G. Fagas, J. C. Greer, and M. A. Ratner, *J. Phys. Chem. C* **113**, 744 (2009).
- [64] L. Venkataraman et al., *Nano Lett.* **6**, 458 (2006).
- [65] M. A. Fox and J. K. Whitesell, *Organic Chemistry*, Jones and Bartlett Publishers, 3rd edition, 2004.
- [66] B. Xu, X. Xiao, and N. Tao, *J. Am. Chem. Soc.* **125**, 16164 (2003).
- [67] D. K. James and J. M. Tour, *Top. Curr. Chem.* **257**, 33 (2005).
- [68] E. A. Weiss, M. R. Wasielewski, and M. A. Ratner, *Top. Curr. Chem.* **257**, 103 (2005).
- [69] Z. Li et al., *Nanotechnology* **18**, 044018 (2007).
- [70] K. Kim, P. Tarakeshwar, and J. Lee, *Chem. Rev.* **100**, 4145 (2000).
- [71] M. Watson, A. Fechtenkotter, and K. Müllen, *Chem. Rev.* **101**, 1267 (2001).
- [72] F. Hoeben, P. Jonkheijm, E. Meijer, and A. Schenning, *Chem. Rev.* **105**, 1491 (2005).
- [73] J. Taylor, M. Brandbyge, and K. Stokbro, *Phys. Rev. B* **68**, 121101 (2003).
- [74] A. Blum et al., *J. Phys. ChemB* **108**, 18124 (2004).
- [75] Y. Selzer et al., *Nano Lett.* **5**, 61 (2005).

- [76] M. Galperin, M. A. Ratner, and A. Nitzan, *J. Phys.: Condens. Matter* **19**, 103201 (81pp) (2007).
- [77] C. A. Hunter and J. K. M. Sanders, *J. Am. Chem. Soc.* **112**, 5525 (1990).
- [78] J. Seminario, A. Zacarias, and J. Tour, *J. Am. Chem. Soc.* **120**, 3970 (1998).
- [79] M. Levitus et al., *J. Am. Chem. Soc.* **123**, 4259 (2001).
- [80] K. Okuyama, T. Hasegawa, M. Ito, and N. Mikami, *J. Phys. Chem.* **88**, 1711 (1984).
- [81] T. Miteva, L. Palmer, L. Kloppenburg, D. Neher, and U. Bunz, *Macromolecules* **33**, 652 (2000).
- [82] J. Kim and T. M. Swager, *Nature* **411**, 1030 (2001).
- [83] H. Li, D. R. Powell, T. K. Firman, and R. West, *Macromolecules* **31**, 1093 (1998).
- [84] C. Wang, A. Batsanov, M. Bryce, and I. Sage, *Org. Lett.* **6**, 2181 (2004).
- [85] D. S. Seferos, S. A. Trammell, G. C. Bazan, and J. G. Kushmerick, *PNAS* **102**, 8821 (2005).
- [86] S. Creager et al., *J. Am. Chem. Soc.* **121**, 1059 (1999).
- [87] B. Schlicke, P. Belser, L. De Cola, E. Sabbioni, and V. Balzani, *J. Am. Chem. Soc.* **121**, 4207 (1999).
- [88] C. Atienza et al., *Chem. Comm.* , 3202 (2006).
- [89] M. Magoga and C. Joachim, *Phys. Rev. B* **56**, 4722 (1997).
- [90] J. K. Tomfohr and O. F. Sankey, *phys. stat. sol. (b)* **233**, 59 (2002).
- [91] R. M. Metzger, *Acc. Chem. Res.* 1999, 32, 950-957 **32**, 950 (1999).
- [92] R. M. Metzger, *J. of Solid State Chem.* **168**, 696 (2002).
- [93] Y. Luo et al., *ChemPhysChem* **3**, 519 (2002).
- [94] J. He et al., *J. Am. Chem. Soc.* **127**, 1384 (2005).

- [95] S. J. van der Molen et al., *Nanotechnology* **17**, 310 (2006).
- [96] T. Kudernac, S. J. van der Molen, B. J. van Wees, and B. L. Feringa, *Chem. Comm.* , 3597 (2006).
- [97] D. I. Gittins, D. Bethell, D. J. Schiffrin, and R. J. Nichols, *Nature* **408**, 67 (2000).
- [98] J. K. Sørensen et al., *Org. Lett.* **8**, 1173 (2006).
- [99] B. Q. Xu, X. L. Li, X. Y. Xiao, H. Sakaguchi, and N. J. Tao, *Nano Letters* **5**, 1491 (2005).
- [100] B. L. Feringa, *Molecular Switches*, Wiley-VCH Verlag GmbH, Weinheim, Germany, 2001.
- [101] W. R. Browne and B. L. Feringa, *Nature Nanotechnology* **1**, 25 (2006).
- [102] N. Weibel, S. Grunder, and M. Mayor, *Org. Biomol. Chem.* **5**, 2343 (2007).
- [103] B. L. Feringa, *J. Org. Chem.* **72**, 6635 (2007).
- [104] X. Guo et al., *Nano Letters* **7**, 1119 (2007).
- [105] X. Xiao, B. Xu, and N. Tao, *Angew. Chem. Int. Ed.* **43**, 6148 (2004).
- [106] J. Liao et al., in preparation .
- [107] M. Bendikov and F. Wudl, *Chem. Rev.* **104**, 4891 (2004).
- [108] M. R. Bryce, *Adv. Mater.* **11**, 11 (1999).
- [109] A. Credi et al., *New J. Chem.* **10**, 1061 (1998).
- [110] P. R. Ashton et al., *J. Am. Chem. Soc* **121**, 3951 (1999).
- [111] J. Ghilane, P. Hapiot, and A. J. Bard, *Anal. Chem.* **78**, 6868 (2006).
- [112] S. A. Getty et al., *Phy. Rev. B* **71**, 241401 (2005).
- [113] D. Andrews et al., *J. Phys. Chem. C* **112**, 16991 (2008).

Appendix A

Overview of investigated molecules

In this thesis, three groups of conjugated molecules have been investigated.

In Chapter 5, we systematically studied the molecular conductance of OPE molecules with different anchor groups: thiols, pyridine nitrogens, and amines. The influences of substituted groups (methoxy) were also discussed.

We measured OPE-monothiols in Chapter 6, and discovered molecular junctions can be efficiently formed by intermolecular π - π interactions.

Finally in Chapter 7, we tried to tune the conductance of two types of redox molecules: TTF and Ferrocene.

	S. Grunder, N. Jenny, V. Horhoiu, Prof. M. Mayor	Department of Chemistry, University of Basel, Switzerland
*	Prof. M. Bryce et al.	Department of Chemistry, University of Durham, UK
†	Dr. Shi-Xia Liu, Prof. Silvio Decurtins et al.	Department of Chemistry and Biochemistry, University of Bern, Switzerland

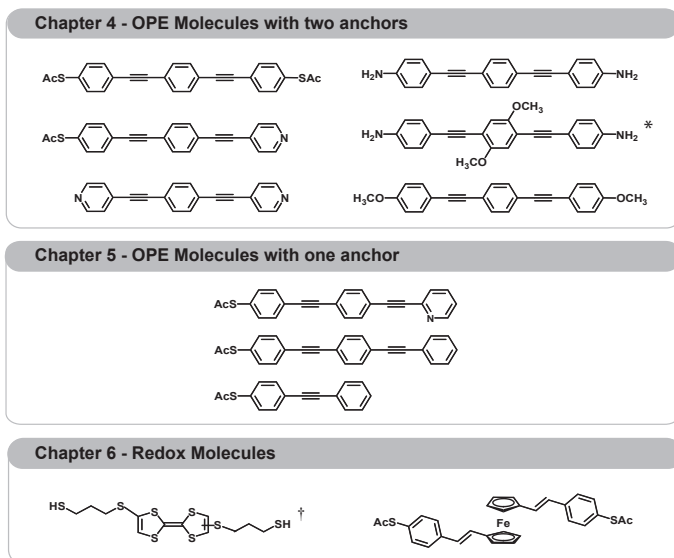


Figure A.1: Overview on the molecules which were investigated in this thesis.

Appendix B

Additional data

B.1 Measurements of OPEs with different anchors

UV-vis spectra of thiol- and pyridine- anchored OPEs

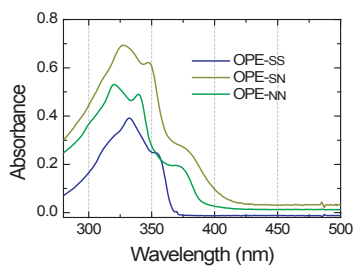


Figure B.1: UV-vis spectra of OPEs with thiol- and pyridine- anchors.

Histograms of OPE-diamines

The molecular signature of OPE-diamine is not as well defined as other anchoring molecules. We observed slightly higher counts than pure solvent in different concentrations and solvents.

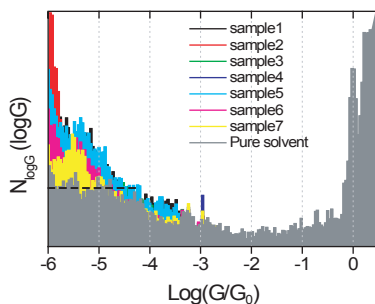


Figure B.2: $\log G$ histograms of OPE-diamine. Measurements of seven samples with different concentrations (0.1 – 10 mM) and solvents (THF:mesitylene = 1:4 v/v-ratio and ethyl benzoate) show slightly higher counts than pure solvent (constant tunneling background in pure solvent is marked by dash line).

B.2 Measurements of OPE- dithiol and monothiols

Linear histograms

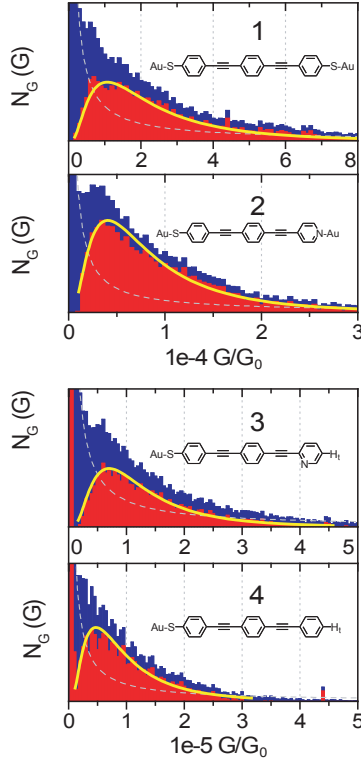


Figure B.3: Linear histograms and subtraction of tunneling background for molecule 1-4. Blue histogram - linear histogram of 0.25 mM molecular solution; Gray dash line - tunneling background of 0.25 mM molecular solution; Red histogram - molecular signal after background subtraction. Yellow line - transformation of Gaussian fitting from log-scale to lin-scale. Single molecule conductance is derived from the peak value.

Individual conductance traces

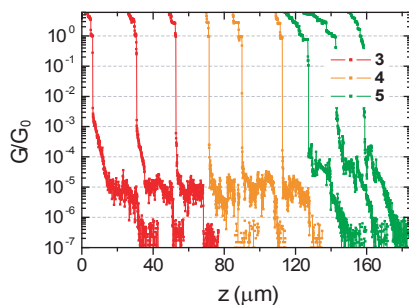


Figure B.4: Single conductance traces $G(z)$ of OPE-monothiol molecules **3-5**. OPE-monothiols with three phenylene unites (molecules **3-4**) can form clear molecular plateaus, while OPE-monothiol with only two phenylene units show visible but shorter and noisier plateaus at higher conductance value.

Histogram of octane-monothiol

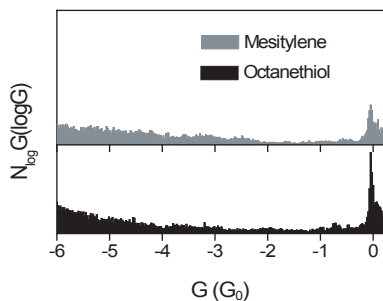


Figure B.5: $\log G$ histograms of solvent (mesitylene) and octanethiol. Octanethiols with weak van der Waals intermolecular interactions behave as passive tunneling media as pure solvent.

B.3 Measurements of TTF-alkanedithiol

Characterization of TTF-alkanedithiol

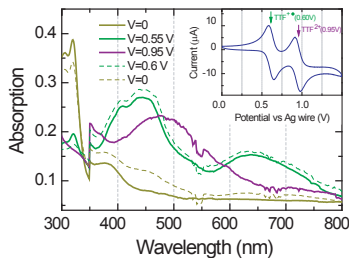


Figure B.6: Characterization of TTF-alkanedithiol with Cyclic voltammogram (inset) and UV-vis absorption by fixing the potential at different redox states of TTF. Cyclic voltammogram shows two reversible oxidation states of TTF (free radical state at neutral TTF (yellow) absorbs at 320 nm; Its radical state (green) shows two absorption bands (peaks at 440 nm and 640 nm); The dication state absorbs at 480 nm. Dash lines show that the process is fully reversible as also indicated by the CV curve.

Histograms of TTF-alkanedithiol in mesitylene

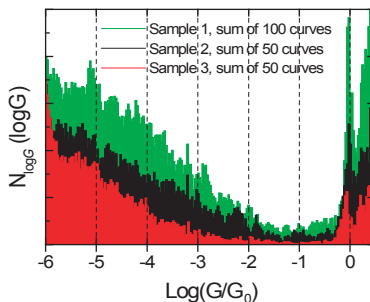


Figure B.7: $\log G$ histograms of 0.6 mM TTF-alkanedithiol in mesitylene.

Appendix C

Technical details

C.1 Sample fabrication

1. **The substrate:** To fabricate sample substrates, we use a flexible spring steel plate, onto which an insulating polyimide layer, several micrometres thick, is cast. At first a 6.5×6.5 cm piece of spring steel is cleaned in an acetone and afterwards isopropanol bath by using of ultrasonic agitation. Then 3 to 4 layers of polyimide (Pyralin PI2610 HD Microsystem) are spun at 8000 rpm for 40 s on top of the metallic plate. After each layer the plate is baked at 200°C for 40 min. Finally, the polyimide-covered plate is cured for 1 hr at 350°C under 10^{-5} mbar. A laser cutting is used (Digipack AG, CH-8623 Wetzikon) to cut the covered steel plate to 24×10 mm sample substrates.
2. **E-beam lithography:** Break junction structures are patterned by e-beam lithography. A layer of ~ 600 nm positive resist (PMMA 950 K, Allresist GmbH, diluted with additional chlorbenzene) is spin-coated onto the substrate (4000 rpm, 40 s), and baked at 175°C for 30 min. After exposure with e-beam, the development is performed in a solution of MIBK (4-methyl-2-pentanone) and isopropanol (1:3 v/v-ratio) for 45 s, followed by a rinse in isopropanol.
3. **Metal deposition:** We next mount the substrates in a vacuum chamber (PLS 500, Balzers-Pfeiffer GmbH) and evacuate down to $\sim 10^{-6}$ mbar. After the sample holder is cooled down to $\sim 0^\circ\text{C}$, we evaporate 10 nm titanium layer at an angle of 50° and 60 nm gold layer perpendicular to the sample holder. This procedure ensures a good adhesion of the gold layer but avoids the presence of titanium in the central region

of the bridge. Lift-off after evaporation is carried out in warm acetone ($\sim 40^\circ$).

4. **Junction protection:** In the case of electrochemical samples, the major part of the Au surface needs to be protected to prevent leakage current. We use polyimide photoresist (HD-4104, HD-microsystem) to cover the junction by standard photolithography. Polyimide photoresist is first spin-coated onto the sample (4000 rpm, 60 s), and baked at 85°C for 2 min followed by at 95°C for 2 min. After exposure and development, the sample is again cured for 1 hr at 350°C under 10^{-5} mbar.
5. **Under-etching:** To obtain a free standing central metal bridge, the polyimide is dry-etched in a reactive ion etching (RIE) machine (PlasmaLab 80 plus, Oxford). During the etching process the contact pads are covered by two glass slides. The exposed polyimide is slowly etched away which results in a hole under the central part of the Au bridge. The etching is performed at a flow of 2% CHF_3 and 32% oxygen under pressure of 0.1 torr and at a power of 100 W for ~ 3 min.

C.2 Deprotection

In our break junction experiments, we use terminal thiols (-SH) to bind target molecules to Au electrodes through the formation of Au-S bonds. However, thiol-anchored conjugated molecules are not stable in air. The bifunctional molecules easily polymerize via disulfide bond formation (-S-S-). Therefore thiols are usually protected by acetyl- groups (-COCH₃). During measurements we need to deprotect them *in situ* to obtain fresh thiols.

The deprotection of an acetyl-protected conjugated thiol can be viewed as a hydrolysis process of an ester catalyzed by a weak base or acid. As illustrated in Fig. C.1, the -S-C- bond breaks and the sulfur atom gains a proton (H⁺) of a water molecule to become a thiol group (-SH) while the acetyl group collects the remaining hydroxyl ion (OH⁻).

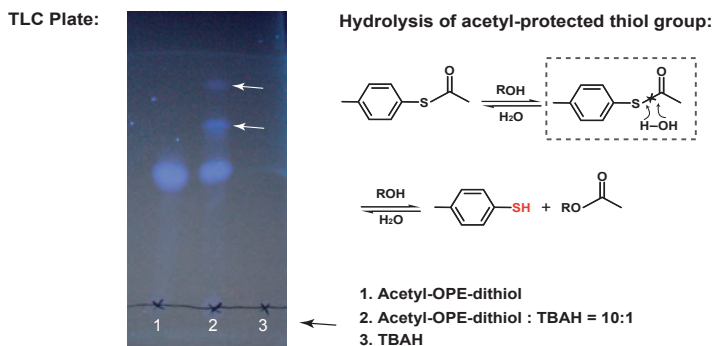


Figure C.1: Illustration of deprotection of acetyl-protected conjugated thiols. Proper conditions for acetyl-protected OPE-dithiols were established via thin layer chromatography (TLC). The plate (under 365 nm UV lamp) shows two new components (see white arrows) as indications of free thiol-anchored OPE molecules in the presence of weak base.

We established proper conditions for the deprotection via thin layer chromatography (TLC), which is a simple, quick, and inexpensive procedure that provides the chemist a quick answer as to how many components are in a mixture.

A TLC plate is a sheet of aluminum which is coated with a thin layer of a solid adsorbent (usually silica or alumina). A small amount of the compound to be analyzed is spotted near the bottom of the plate. As marked in Fig. C.1, spot 1 is the acetyl-OPE-dithiol (dissolved in DCM). After

adding in $\sim 10\%$ (mol) of TBAH (tetrabutylammonium hydroxide, dissolved in THF), the mixture is spotted at position **2**. TBAH is also spotted at position **3** as a comparison. The plate is then placed in a shallow pool of a solution (cyclohexane:DCM = 1:1 v/v-ratio) so that only the very bottom of the plate is in the liquid. This liquid slowly rises up the TLC plate by capillary effect. As the solvent moves past the spot that was applied, the compounds in the mixture are separated due to different solubility and adsorption strength to the adsorbent. The plate is then removed from the developing chamber, dried, and the conjugated components can be visualized under a UV lamp.

The TLC plate (Silica gel 60 F₂₅₄ on aluminum sheets, MERCK) shows clearly two new components after deprotection which move higher up the plate (see white arrows). These are the hints of thiol-anchored OPE molecules, possibly the top one has free thiols on both ends and second-top one has free thiol only on one end.

During deprotection, it is important to keep the solution under Ar in order to prevent the formation of disulfide bonds. It can be observed on a TLC plate that the polymerized compounds are difficult to move up and remain at the spotted position.

C.3 Fabrication of Pt/Ppy quasi-reference electrode

The Pt/Ppy reference electrode used in the electrochemical measurement is fabricated by cyclic voltammetry (CV) (50 scan cycles) with a Pt wire as working electrode in an acetonitrile solution containing of 10 mM pyrrole and 0.1 M Bu_4NPF_6 electrolyte (tetrabutylammonium hexafluoro-phosphate).

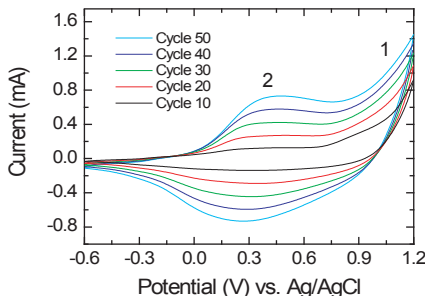


Figure C.2: Electrodeposition of polypyrrole by cyclic voltammetry.

The evolved CV scans (Fig. C.2) show the electrodeposition of polypyrrole. Current increase trend at **1** (at potentials > 0.7 V) corresponds to the polymerization of pyrrole monomers. Current peak **2** indicates the oxidation of polypyrrole. After several scans, one could observe a black polypyrrole coating layer on the Pt wire.

In the final step, one has to perform an extra scan during which the potentiostat is turned off at 0.4 V versus Ag/AgCl. At this point, the polypyrrole is partially oxidized to produce a film of $\text{PPy}/\text{PPy}^+\text{PF}_6^-$ on the Pt wire. This is important for the conducting polymer to maintain a relatively stable potential in an electrochemical cell. Although there is still some potential shift in experiments ($\sim \pm 0.2$ V), this complex reference electrode is much more stable compared with a bare metal wire.

Appendix D

Publication List

Articles

- S. Wu, R. Huber, J. Brunner, M. T. González, S. Grunder, M. Mayor, C. Schönenberger and M. Calame, *The role of contacts in molecular conductance: a comparison between thiol and pyridine*, in preparation.
- J. Liao, Jon S. Agustsson, S. Wu, C. Schönenberger, M. Calame, S. X. Liu and S. Decurtins, *Cyclic conductance switching in networks of redox-active molecular junctions*, to be published.
- S. Wu, M. T. González, R. Huber, S. Grunder, M. Mayor, C. Schönenberger and M. Calame, *Molecular Junctions based on Aromatic Coupling*, Nature Nanotech. **3**, 569 (2008)
- R. Huber, M. T. González, S. Wu, M. Langer, S. Grunder, V. Horhoiu, M. Mayor, M. Bryce, C. Wang, R. Jitchati, C. Schönenberger and M. Calame, *Electrical conductance of conjugated oligomers at the single molecule level*, JACS **130**, 1080 (2008).
- Z. M. Wu, S. Wu, S. Oberholzer, M. Steinacher, M. Calame and C. Schönenberger, *Scaling of 1/f noise in tunable break-junctions*, Appl. Phys. Rev. B **78**, 235421(2008).
- M. T. González, J. Brunner, R. Huber, S. Wu, C. Schönenberger and M. Calame, *Conductance values of alkanedithiol molecular junctions*, New J. Phys. **10**, 065018 (2008)
- M. T. González, S. Wu, R. Huber, S. J. van der Molen, C. Schönenberger and M. Calame, *Electrical Conductance of Molecular Junctions by a Robust Statistical Analysis*, Nano Letters **6**, 2238 (2006).

Poster contributions

- *The role of contacts in molecular conductance: a comparison between thiol and pyridine*
S. Wu, R. Huber, M. T. González, J. Brunner, S. Grunder, M. Mayor, C. Schönenberger and M. Calame,
SwissNano Workshop 2009, Basel, Switzerland, Jun. 11th-12th, 2009.
- *Break Junctions in Liquid for Molecular Electronics*
S. Wu, M. T. González, R. Huber, S. Grunder, M. Mayor, S. X. Liu and S. Decurtins, C. Schönenberger and M. Calame.
The 3rd AGEF - Euregio Workshop on Interfacial Electrochemistry, Rolduc Abbey, Kerkrade, Netherlands, Jun. 2nd - 3rd, 2008.
- *Aromatic Induced Single Molecular Junctions*
S. Wu, R. Huber, M. T. González, S. Grunder, M. Mayor, C. Schönenberger and M. Calame.
Annual Meeting of the Swiss Physical Society, Geneva, Switzerland, Mar. 26th, 2008.
- *Break Junctions in liquid for molecular electronics*
R. Huber, S. Wu, M. T. González, H. Breitenstein, P. Reimann, C. Schönenberger and M. Calame.
International Workshop on Molecular Electronics, Řež, Prague, Czech Republic, Jun. 30th - July 4th, 2006.

Oral presentations

- *The Role of Contacts in Molecular Conductance*
Swiss Workshop on Molecular Electronics, University of Bern, Switzerland, May 12th, 2009.
- *Molecular Junction Based on Aromatic Coupling*
The 4th International Conference on Molecular Electronics: ELEC-MOL'08, Grenoble, France, Dec. 8th-12th 2008.
- *Break Junctions in Liquid for Molecular Electronics*
The 3rd AGEF - Euregio Workshop on Interfacial Electrochemistry, Rolduc Abbey, Kerkrade, Netherlands, Jun. 2nd - 3rd, 2008.
- *Statistical Analysis of Single-Molecular-Junctions Conductance*
NCCR Nano Meeting, PSI Villigen, Switzerland, Nov. 15th, 2006

Appendix E

Curriculum Vitae

Education

- 2005-present
Ph.D. study in Nanoscience, Department of Physics, University of Basel, Switzerland. Thesis: *Electrical conductance of single conjugated oligomers*. Supervisor: Prof. Dr. C. Schönenberger.
- 2005
M.Sc. in Material Science (Material Physics), Faculty of Engineering, Christian-Albrechts-University of Kiel, Germany. Thesis: *Trenched metallized carbon nanotube composites for potential hydrogen sensor application*. Supervisor: Prof. Dr. R. Adelung
- 2003
M.Eng. in Material Science (Material Chemistry), Lab of Information Recording Materials, Beijing Institute of Graphic Communication, P. R. China. Thesis: *Synthesis and characterization of an acid-catalyzed hydrophilic-to-hydrophobic switching polymer*. Supervisor: Prof. Dr. J.-L. Pu
- 2000
B.Eng. in Polymer Materials and Engineering, Faculty of Chemical Engineering, Beijing Institute of Petrochemical Technology, P. R. China.

Teaching experience

- 2008-2009 summer semesters
Practical course *Molecular Physics*
- 2008 summer semester
Practical course for high school students
Quantized Conductance in Atomic Contacts
- 2006-2007 summer semesters
Practical course *Cyclic Voltammetry*
- 2006-2009 spring semesters
Practical course *General Physics for Beginners*

Awards

- 2009
Camille und Henry Dreyfus-Stipendium
- 2009
Chinese Government Award For Outstanding Self-financed Students
Abroad

Acknowledgements

I would like to thank here all the people who have helped me on this both painful and enjoyable journey of pursuing a Ph.D..

First and foremost, I express my sincere gratitude to Prof. Dr. Christian Schönenberger, an inspiring and trusted supervisor, for giving me the opportunity to work on this challenging topic and showing me a way to explore the secrets of nature. Thank you for providing continuous guidance, advice and support throughout the whole work.

I am deeply grateful to all the break junction team members: senior scientist Dr. Michel Calame, for your theoretical and experimental guidance, fruitful discussions and your constant care; Dr. Teresa González and Dr. Roman Huber for your great contributions in building the setup and for sharing the knowledge of data analysis; Jan Brunner and Toni Fröhlich, our new members, for interesting discussions as well as your fresh mood. I would also like to thank all the current and former members of the Nano-electronics group for a friendly atmosphere.

I am thankful to our excellent chemists in Prof. Dr. Marcel Mayors' group, especially Sergio Grunder, who actively synthesized most of molecules for our measurement and Yann Leroux, who brought the knowledge of electrochemistry. I did not forget William Kylberg and Verena Thommen, for your help on electrochemistry and photoelectrochemistry at my beginning stage. It is always cheerful to come over to discuss molecules with you.

Special thanks go to our mechanics workshop, Heinz Breitenstein and Silvester Jakob, for improving our setup, and electronics workshop around Michael Steinacher for the development of unique electronic devices.

Let me personally thank my hero, Jie Zeng, for your courage to face changes, your optimism during hard time and the joys and dynamics you bring to our life. I am very much indebted to my parents, for your tremen-

dous but silent understanding and support.

Finally I would like to thank the financial support provided by the NCCR on Nanoscale Science.